



Publication Year	2015
Acceptance in OA @INAF	2020-03-03T08:57:35Z
Title	βγ [C II] 158 μm Emission as a Star Formation Tracer
Authors	Herrera-Camus, R.; Bolatto, A. D.; Wolfire, M. G.; Smith, J. D.; Croxall, K. V.; et al.
DOI	10.1088/0004-637X/800/1/1
Handle	http://hdl.handle.net/20.500.12386/23082
Journal	THE ASTROPHYSICAL JOURNAL
Number	800

[C II] 158 μm EMISSION AS A STAR FORMATION TRACER

R. HERRERA-CAMUS^{1,2}, A. D. BOLATTO^{1,2}, M. G. WOLFIRE¹, J. D. SMITH³, K. V. CROXALL⁴, R. C. KENNICUTT⁵, D. CALZETTI⁶,
 G. HELOU⁷, F. WALTER⁸, A. K. LEROY⁹, B. DRAINE¹⁰, B. R. BRANDL¹¹, L. ARMUS¹², K. M. SANDSTROM¹³, D. A. DALE¹⁴,
 G. ANIANO¹⁵, S. E. MEIDT⁸, M. BOQUIEN⁵, L. K. HUNT¹⁶, M. GALAMETZ¹⁷, F. S. TABATABAEI⁸, E. J. MURPHY⁷,
 P. APPLETON¹⁸, H. ROUSSEL¹⁹, C. ENGELBRACHT^{20,21,23}, AND P. BEIRAO²²

¹ Department of Astronomy, University of Maryland, College Park, MD 20742, USA

² Laboratory for Millimeter-Wave Astronomy, University of Maryland, College Park, MD 20742, USA

³ Department of Physics and Astronomy, University of Toledo, 2801 West Bancroft Street, Toledo, OH 43606, USA

⁴ Department of Astronomy, The Ohio State University, 4051 McPherson Laboratory, 140 West 18th Avenue, Columbus, OH 43210, USA

⁵ Institute of Astronomy, University of Cambridge, Madingley Road, Cambridge CB3 0HA, UK

⁶ Department of Astronomy, University of Massachusetts, Amherst, MA 01003, USA

⁷ Infrared Processing and Analysis Center, California Institute of Technology, Pasadena, CA 91125, USA

⁸ Max-Planck-Institut für Astronomie, Königstuhl 17, D-69117 Heidelberg, Germany

⁹ National Radio Astronomy Observatory, 520 Edgemont Road, Charlottesville, VA 22903, USA

¹⁰ Department of Astrophysical Sciences, Princeton University, Princeton, NJ 08544, USA

¹¹ Leiden Observatory, Leiden University, P.O. Box 9513, 2300-RA Leiden, The Netherlands

¹² Spitzer Science Center, California Institute of Technology, MC 314-6, Pasadena, CA 91125, USA

¹³ Steward Observatory, University of Arizona, 933 North Cherry Avenue, Tucson, AZ 85721, USA

¹⁴ Department of Physics and Astronomy, University of Wyoming, Laramie, WY 82071, USA

¹⁵ Institut d'Astrophysique Spatiale, CNRS (UMR8617) Université Paris-Sud 11, Batiment 121, Orsay, France

¹⁶ INAF-Osservatorio Astrofisico di Arcetri, Largo E. Fermi 5, I-50125 Firenze, Italy

¹⁷ European Southern Observatory, Karl Schwarzschild Strasse 2, D-85748 Garching, Germany

¹⁸ NASA Herschel Science Center, IPAC, California Institute of Technology, Pasadena, CA 91125, USA

¹⁹ Institut d'Astrophysique de Paris, Université Pierre et Marie Curie, CNRS UMR 7095, F-75014 Paris, France

²⁰ Steward Observatory, University of Arizona, Tucson, AZ 85721, USA

²¹ Raytheon Company, 1151 East Hermans Road, Tucson, AZ 85756, USA

²² Observatoire de Paris, 61 avenue de l'Observatoire, F-75014 Paris, France

Received 2014 July 3; accepted 2014 September 20; published 2015 February 7

ABSTRACT

The [C II] 157.74 μm transition is the dominant coolant of the neutral interstellar gas, and has great potential as a star formation rate (SFR) tracer. Using the *Herschel* KINGFISH sample of 46 nearby galaxies, we investigate the relation of [C II] surface brightness and luminosity with SFR. We conclude that [C II] can be used for measurements of SFR on both global and kiloparsec scales in normal star-forming galaxies in the absence of strong active galactic nuclei (AGNs). The uncertainty of the $\Sigma_{[\text{C II}]} - \Sigma_{\text{SFR}}$ calibration is ± 0.21 dex. The main source of scatter in the correlation is associated with regions that exhibit warm IR colors, and we provide an adjustment based on IR color that reduces the scatter. We show that the color-adjusted $\Sigma_{[\text{C II}]} - \Sigma_{\text{SFR}}$ correlation is valid over almost five orders of magnitude in Σ_{SFR} , holding for both normal star-forming galaxies and non-AGN luminous infrared galaxies. Using [C II] luminosity instead of surface brightness to estimate SFR suffers from worse systematics, frequently underpredicting SFR in luminous infrared galaxies even after IR color adjustment (although this depends on the SFR measure employed). We suspect that surface brightness relations are better behaved than the luminosity relations because the former are more closely related to the local far-UV field strength, most likely the main parameter controlling the efficiency of the conversion of far-UV radiation into gas heating. A simple model based on *Starburst99* population-synthesis code to connect SFR to [C II] finds that heating efficiencies are 1%–3% in normal galaxies.

Key words: galaxies: ISM – galaxies: star formation – infrared: galaxies – ISM: structure

1. INTRODUCTION

The [C II] 157.74 μm fine-structure transition ($^2P_{3/2} - ^2P_{1/2}$) is one of the brightest emission lines in star-forming galaxies (Stacey et al. 1991, 2010) and a major coolant for the neutral atomic gas (Wolfire et al. 2003). In this phase of the interstellar medium (ISM), far-ultraviolet (FUV) photons produced by O and B stars heat the gas via the photoelectric effect on small dust grains and polycyclic aromatic hydrocarbons (PAHs; Helou et al. 2001). The ejected photoelectrons are thermalized and heat the gas. Neutral collisions marginally dominate the excitation of the fine-structure level of singly ionized carbon atoms and the gas cools by emission of [C II] 158 μm photons. This chain of events provides a link between the star formation activity and

the [C II] emission: if the gas is in thermal balance, and it is cooled mainly by 158 μm emission, the [C II] line measures the total energy that is put into the gas by star formation activity.

The ionization potential of neutral carbon is 11.3 eV, so ionized carbon (C^+) can be found in phases of the ISM where hydrogen is in molecular, neutral atomic, or ionized form. C^+ can be excited by collisions with electrons (e^-), hydrogen atoms (H), and molecules (H_2). Assuming collisional excitation, the [C II] integrated line intensity ($I_{[\text{C II}]}$) in the optically thin limit is (Crawford et al. 1985)

$$I_{[\text{C II}]} = 2.3 \times 10^{-24} \left[\frac{2e^{-91.2/T}}{1 + 2e^{-91.2/T} + n_{\text{crit}}/n} \right] N_{\text{C}^+}, \quad (1)$$

where $I_{[\text{C II}]}$ is in units of $\text{W m}^{-2} \text{sr}^{-1}$, T is the kinetic temperature in K, n is the volume density of the collisional partner (H, H_2 ,

²³ Deceased 2014 January 8.

or e^- in cm^{-3} , N_{C^+} is the column density of C^+ in cm^{-2} , and n_{crit} is the critical density for collisions with a given partner in cm^{-3} . The latter is a function of temperature. For a typical cold neutral medium (CNM) temperature of $T \approx 100$ K (Heiles & Troland 2003; Wolfire et al. 2003), the critical density for collisions with e^- and H is 9 cm^{-3} and 3000 cm^{-3} , respectively (Goldsmith et al. 2012). Typical volume densities of H atoms in the CNM are $n_{\text{H}} \approx 50 \text{ cm}^{-3}$ ($\ll n_{\text{crit}}(\text{H})$) and the fractional ionization $n_{e^-}/n_{\text{H}} \lesssim 10^{-3}$, so in this phase collisions with H atoms dominate the C^+ excitation. In the dense gas interface between molecular clouds and H II regions—also known as photodissociation regions (PDRs)—the excitation is dominated by collisions with molecular hydrogen. At a gas temperature of 100 K, the critical density for collisions with H_2 is 6100 cm^{-3} (Goldsmith et al. 2012). In the warm ionized medium (WIM), for a characteristic temperature of $T \approx 8000$ K (McKee & Ostriker 1977; Haffner et al. 1999), the critical density for collisions with e^- is 44 cm^{-3} (Goldsmith et al. 2012). For a range of electron densities in the WIM of $\sim 0.08\text{--}0.4 \text{ cm}^{-3}$ (Haffner et al. 2009; Velusamy et al. 2012), collisions with e^- are responsible for the excitation of C^+ .

The multiphase contribution to the [C II] emission includes the CNM, PDRs, H II regions, and the WIM (Stacey et al. 1985, 2010; Shibai et al. 1991; Bennett et al. 1994; Pineda et al. 2013). The individual contribution of each one of these ISM components to the total [C II] luminosity is still a matter of study and depends on the nature of the object, location, and resolution of the observations. In the Galactic plane, early observations by the *COsmic Background Explorer* show that the [C II] emission tends to follow the spiral arms and peaks at the molecular ring (Wright et al. 1991; Bennett et al. 1994). More recently, Pineda et al. (2013), based on the *Herschel*/HIFI project “Galactic Observations of Terahertz C^+ ”, also find that in the plane of the galaxy the [C II] emission is mostly associated with the spiral arms, with dense PDRs as the main source of the total [C II] emission ($\sim 47\%$), followed by atomic gas ($\sim 21\%$) and small contributions from the ionized gas ($\sim 4\%$). In low-metallicity galaxies, the PDR contribution to the [C II] emission can be dominant (80% in IC 10; Madden et al. 1997) or small (10% in Haro 11; Cormier et al. 2012). Moving to higher redshifts, Stacey et al. (2010) find that for three starburst systems in the redshift range $z \sim 1\text{--}2$ the origin of the [C II] emission is also dominated by the PDR component, with the ratio of the [C II] to the FIR emission similar to what is measured in nearby starburst galaxies.

Previous studies have searched for the connection between [C II] emission and star formation activity. One of the first surveys of nearby, gas rich spirals observed in the [C II] transition was done by Stacey et al. (1991) using the Kuiper Airborne Observatory (KAO). They find that the integrated [C II]/ $^{12}\text{CO}(1\text{--}0)$ line intensity ratio for starburst nuclei is similar to the ratio measured in Galactic OB star-forming regions. They also measure ratios a factor ~ 3 smaller in non-starburst systems and therefore proposed to use this ratio as a tool to characterize the star formation activity. With the advent of the *Infrared Space Observatory* (ISO), Boselli et al. (2002) derive one of the first calibrations of the star formation rate (SFR) based on the [C II] luminosity ($L_{[\text{C II}]}$). For a sample of 22 late-type galaxies including galaxies from the Virgo Cluster and M82, they find a nonlinear relationship between $H\alpha$ and [C II] global luminosities ($L_{H\alpha} \propto L_{[\text{C II}]}^{0.79}$) with a dispersion of at least a factor of ~ 3 . Also using ISO [C II] observations, De Looze et al. (2011) find a nearly linear correlation between

SFR(FUV+24 μm) and $L_{[\text{C II}]}$ with a dispersion of ~ 0.3 dex for a sample of 24 local, star-forming galaxies.

More evidence in favor of [C II] emission as a star formation tracer comes from *Herschel* observations. Mookerjea et al. (2011) find that the [C II] emission in the M33 HII region, BCLMP 302, strongly correlates with $H\alpha$ and dust continuum emission on scales of ~ 50 pc. More recently, Sargsyan et al. (2012), De Looze et al. (2014), and Pineda et al. (2014) explore the [C II]–SFR connection in luminous infrared galaxies (LIRGs, $L_{\text{IR}} > 10^{11} L_{\odot}$), dwarf galaxies, and the Milky Way, respectively. Sargsyan et al. (2012) find a linear relationship between the SFR(FIR) and $L_{[\text{C II}]}$ for a sample of 24 LIRGs. De Looze et al. (2014), using the Dwarf Galaxy Survey (Madden et al. 2013), conclude that the [O I] 63 μm line is a better SFR tracer than [C II] in low-metallicity galaxies. Pineda et al. (2014) find that [C II] emission emerging from different phases of the ISM in the Milky Way correlates well with SFR at Galactic scales.

The [C II] transition presents many advantages as an SFR indicator. Among these: (1) it is a very bright line, with luminosities typically $\sim 0.1\%\text{--}1\%$ of the FIR luminosity; (2) it is practically unaffected by extinction—possible exceptions include edge-on galaxies (Heiles 1994) and extreme starbursts (Luhman et al. 1998); (3) it can be used to study star-forming galaxies at redshifts $z \gtrsim 1$ using ground-based observatories like the Atacama Large Millimeter Array (ALMA) (e.g., see Figure 8). For many of these high-redshift objects, the [C II] luminosity might be one of the few available tools to measure SFRs.

The so-called [C II] deficit is the most important potential limitation for using [C II] as an SFR indicator. Observed in luminous and ultraluminous infrared galaxies (U/LIRGs; Malhotra et al. 1997, 2001; Brauher et al. 2008; Graciá-Carpio et al. 2011; Díaz-Santos et al. 2013) and nearby galaxies (Beirão et al. 2012; Croxall et al. 2012), the “[C II] deficit” corresponds to lower [C II] to FIR ratios measured as a function of increasingly warm infrared color. Several explanations for the observed low ratio of [C II] to FIR have been proposed over the years. Some of these explanations may account only for a small subset of the low ratios: [C II] self absorption, high dust extinction, softer UV radiation coming from older stellar populations (see Malhotra et al. 2001, for more discussion of these scenarios). Other alternatives seem to be applicable to a larger range of environments. (1) *Charging of the dust grains*: at high radiation fields, the dust grains become positively charged (Malhotra et al. 1997; Croxall et al. 2012). A higher charge implies a higher Coulomb barrier for the photoelectrons to overcome; as a result the photoelectric heating efficiency drops. (2) *[O I] as an additional cooling channel*: if the FUV radiation field and the density of the atomic gas increases above the critical density for collisional excitation with H atoms ($n_{\text{crit}} \sim 10^3 \text{ cm}^{-3}$), then collisional de-excitations start to suppress the [C II] emission and the contribution to the cooling by the [O I] 63 μm line ($n_{\text{crit}} \sim 10^5 \text{ cm}^{-3}$) becomes dominant. (3) *High ionization parameter* (Graciá-Carpio et al. 2011): in H II regions with high ionization parameter, a larger fraction of the non-ionizing stellar UV is absorbed by dust in the H II region, and thus a smaller fraction of the UV photons are available to heat the neutral gas.

The goal of this paper is to derive an accurate [C II]–SFR calibration for normal galaxies, obtain a deeper understanding of the origin of the [C II]–SFR correlation, and identify the limits of applicability of the calibration. To do this, we use a large sample of resolved extragalactic regions—with a median size

of ~ 0.5 kpc—selected from 46 nearby galaxies that are part of the KINGFISH sample of galaxies (Kennicutt et al. 2011, Key Insights on Nearby Galaxies: A Far-Infrared Survey with *Herschel*). This, combined with the wealth of ancillary data available—such as IR, $H\alpha$, and FUV observations—allow us to probe different timescales and environments associated with the star formation activity.

This paper is organized as follows. In Section 2 we describe the KINGFISH sample and the supplementary data. In Section 3 we present the correlations between [C II] and SFR estimated from $24\ \mu\text{m}$, total infrared (TIR), $H\alpha$, and FUV data. We also describe how we removed the cirrus and active galactic nucleus (AGN) contributions to the $24\ \mu\text{m}$ emission. In Section 4 we analyze the scatter of the [C II]–SFR correlation in terms of the IR color and other properties of the ISM derived from the Draine & Li (2007) model. We also compare our calibration to previous [C II]–SFR calibrations derived based on *ISO* and *Herschel* samples. Finally, we use the *Starburst99* code to analyze the scatter in terms of a combination of the duration of the star formation activity and the photoelectric heating efficiency of the dust grains.

2. MAIN SAMPLE DESCRIPTION

We focus our study on 46 galaxies from the KINGFISH sample (Kennicutt et al. 2011). KINGFISH combines deep *Herschel* infrared imaging with spectroscopy of the key ISM diagnostic lines: [C II] $158\ \mu\text{m}$, [N II] $122\ \mu\text{m}$ & $205\ \mu\text{m}$, [O I] $63\ \mu\text{m}$, and [O III] $88\ \mu\text{m}$. Our spectroscopic sample includes 40 spiral galaxies that encompass the full range of late-type morphologies, as well as four irregulars (Holmberg II, NGC 2915, NGC 3077, and NGC 5408), and two ellipticals (NGC 855 and NGC 3265).

There are eight other KINGFISH galaxies with spectroscopic data available that we do not include in this study. These are: NGC 1266, NGC 1316, NGC 1097, NGC 1377, NGC 1404, NGC 4594, NGC 4631, and NGC 4559. The reasons why we exclude these galaxies are presented in Appendix A.

Our sample spans more than three orders of magnitude in TIR luminosity ($L_{\text{TIR}} \sim 10^{7.6} - 10^{11} L_{\odot}$) and about one order of magnitude in distance ($D \sim 2.8 - 26.5$ Mpc). The sample also covers a metallicity range of $12 + \log(\text{O}/\text{H}) \sim 7.72 - 8.77$, measured by Moustakas et al. (2010) using the Kobulnicky & Kewley (2004) calibration. The beam size of the [C II] $158\ \mu\text{m}$ data is $\sim 12''$; given the range of distances, our sample covers a range of spatial resolutions that goes from ~ 0.2 kpc for IC 2574 to ~ 1.5 kpc for NGC 5713, with a median value of 0.6 ± 0.3 kpc. In order to allow comparison between regions with different sizes, we report our measurements as luminosities per unit of physical area (surface brightness or luminosity surface density).

The FIR spectroscopic line observations were carried out with the Photodetector Array Camera & Spectrometer (PACS) on board *Herschel* as part of the *Herschel* key program KINGFISH. The spectral observations were reduced using the *Herschel* Interactive Processing Environment (HIPE) version 11.0. The reduced cubes were then processed to obtain zero, first, and second moment maps. For a detailed description on the reduction and processing of the KINGFISH FIR spectral maps we refer to Croxall et al. (2013). About half of the images consists of strip maps, in some cases including extranuclear regions; the other half corresponds to rectangular regions centered on the nucleus of the galaxy.

The work in this paper is based on the [C II] line, the brightest emission line in our sample. About 70% of the galaxies in our

sample show [C II] line emission above the 3σ level in at least 70% of the map. Figure 1 shows [C II] surface brightness maps and $24\ \mu\text{m}$ continuum contours for four KINGFISH galaxies: NGC 2915, an irregular low-metallicity galaxy with the lowest TIR luminosity in our sample; NGC 4736, a spiral galaxy with a well-defined circumnuclear ring visible in both, [C II] and $24\ \mu\text{m}$ emission; and NGC 5055 and NGC 7793, two flocculent spiral systems with extended [C II] emission detected across the disk and extranuclear regions. At this spatial scale, there is a very good agreement between the [C II] line and the $24\ \mu\text{m}$ dust continuum emission, a well-characterized indicator of SFR.

In order to study the reliability of the [C II] $158\ \mu\text{m}$ line emission as an SFR tracer, it is crucial to combine this FIR line with archival data that provide information about the dust, gas, and young stellar population. In Appendix B we describe the supplementary data used in our analysis, which includes ground-based $H\alpha$, *Galaxy Evolution Explorer* (GALEX) FUV, and *Spitzer* and *Herschel* infrared data. We also use maps of dust properties, like the ones presented in Aniano et al. (2012), based on the Draine & Li dust model (Draine & Li 2007, hereafter DL07).

2.1. Methods

The native pixel size of the [C II] maps after the reduction process was $2''.7$. We regrid the maps in order to define a new pixel size that is roughly the size of the [C II] beam, i.e., $12''$. Among our data, the [C II] maps have the lowest resolution, so we convolve all the other maps from the supplementary data to the [C II] PSF. For this task, we use a library of convolution kernels for the cameras of the *Spitzer*, *Herschel Space Observatory*, GALEX, and ground-based telescopes constructed by Aniano et al. (2011). After this step, we regrid the convolved maps to be aligned with the [C II] maps.

For all the surface brightness and SFR surface density values, we correct for inclination by a factor of $\cos i$.

3. RESULTS

Our goal is to study if the [C II] line can be used as an SFR tracer. To do this we compare the [C II] line emission to four widely used SFR tracers: $H\alpha$, FUV, $24\ \mu\text{m}$, and TIR emission. $H\alpha$ and FUV provide measures of star formation through the rate of production of ionizing photons and the photospheric emission from O and B stars, respectively. The $24\ \mu\text{m}$ and TIR dust emission yields a measure of star formation via the reprocessing of light by dust in star-forming regions. Combination of these tracers is useful to account for the obscured (traced by $24\ \mu\text{m}$ or TIR) and unobscured (traced by $H\alpha$ or FUV) contributions produced by star-forming regions.

3.1. [C II] – $24\ \mu\text{m}$ Correlation

We start our analysis with the $\Sigma_{[\text{C II}]} - \Sigma_{24\ \mu\text{m}}$ correlation because we have $24\ \mu\text{m}$ images available for all the galaxies in our sample. Figure 2 shows this correlation for 4142 regions selected from KINGFISH galaxies. Three sigma upper limits for [C II] emission are shown as dark red triangles.

The $24\ \mu\text{m}$ continuum emission is thought to be primarily produced by small hot dust grains in diffuse regions, transiently heated by the interstellar radiation field. One important contributor to the dust heating are young, hot stars (e.g., Law et al. 2011); however, contribution from older stellar populations cannot be ignored. For example, in M 31, old stars contribute to the heating of the dust in star-forming regions in the disk (Draine et al. 2014) and dominate the heating in the bulge (Groves et al.

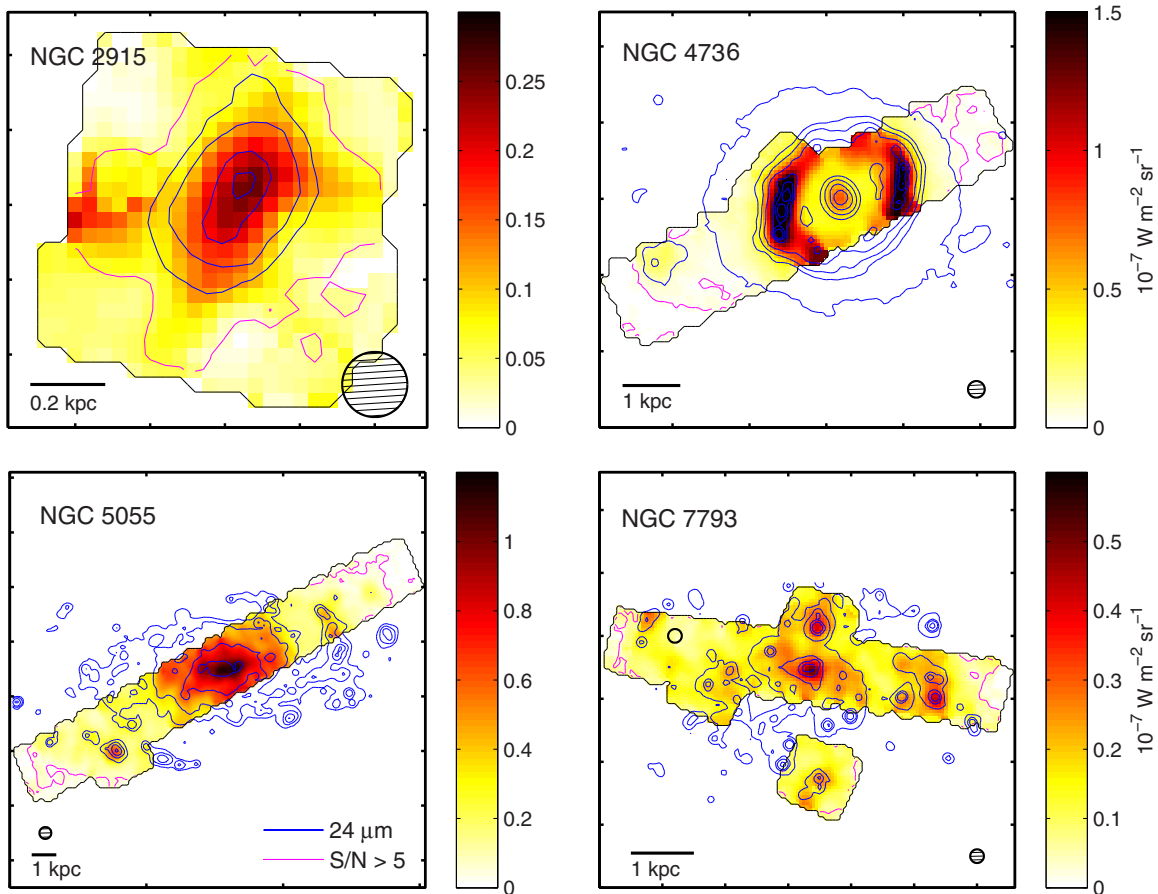


Figure 1. PACS [C II] 158 μm images for four galaxies selected from the KINGFISH sample. The black contours delineate the areas which have [C II] data. The physical scale and the size of the $\sim 12''$ beam are shown in the corners. The color scale shows the [C II] surface brightness in units of $\text{W m}^{-2} \text{sr}^{-1}$ and the blue contours show the 24 μm dust continuum emission. At this spatial scale, there is a very good agreement between the [C II] line and the 24 μm continuum emission. The area enclosed by the magenta contours corresponds to the parts of the galaxy where the S/N of the [C II] emission is greater than 3. The four galaxies in the image are as follows. Top left: NGC 2915, a blue compact dwarf galaxy, and one of the four systems in our sample with metallicity $12+\log(\text{O}/\text{H}) < 8.1$. This galaxy also has the lowest TIR luminosity of the sample ($L_{\text{TIR}} = 3.9 \times 10^7 L_{\odot}$). Top right: NGC 4736, an early-type spiral galaxy with a circumnuclear ring traced by both, [C II] and 24 μm emission. Bottom left: NGC 5055, a spiral (SABc) galaxy. The detected [C II] emission along the disk covers more than one order of magnitude in surface brightness. Bottom right: NGC 7703, a flocculent spiral with [C II] emission mapped using a strip section and one extranuclear regions.

2012). In addition, non-stellar contribution to the radiation field by AGNs can also be an important source of heating of dust grains (Dale et al. 2006; Deo et al. 2009). Given that our plan is to use the 24 μm to trace the young star formation that is reprocessed by dust, in the following section we describe how we account and correct for the 24 μm component that is not associated with star formation activity.

3.1.1. AGN Contribution

X-ray photons produced by the AGN heat the surrounding dust and gas creating X-ray dominated regions (XDRs), (Maloney et al. 1996); as a result, XDRs can contribute to the total [C II] and 24 μm dust emission. Even though by design of the sample the global luminosity of the KINGFISH galaxies is not dominated by AGNs, the effect of the XDRs can be important in the central portions of galaxies. According to the nuclear spectral classification by Moustakas et al. (2010), 19 of the 49 galaxies in our sample are optically classified as AGNs and two other as mixed systems (SF/AGN). Another six galaxies that show no AGN signature in the optical have nuclear X-ray measured fluxes that may indicate AGN activity (Tajer et al. 2005; Grier et al. 2011). To study the effect of the AGN, we select the central region using circular apertures of ~ 0.5 kpc radius. For galaxies further than ~ 17 Mpc, the central $12''$ region is

larger than 1 kpc; thus, for these cases we only mask the central $12''$ region.

The size of this aperture should be enough to enclose the emission arising from the XDRs powered by the AGN. The left panel on Figure 2 shows the properties of the AGN-selected regions (color diamonds and squares) and star-forming regions (gray dots) in the [C II] – 24 μm surface brightness plane. The AGN-selected regions are color coded according to the nucleus classification: optically selected AGNs (red) and X-ray selected AGNs (green). About half of the AGN-selected regions tend to show a 24 μm excess compared to [C II] (or a [C II] deficit compared to 24 μm); in the most extreme cases, the excess can be as high as a factor of ~ 6 (e.g., regions from NGC 4736; see Figure 13 in Appendix F for individual correlations). It is likely that these higher 24 μm – [C II] ratios are caused by (1) the AGN contributing more to the dust continuum than to the [C II] emission; (2) a reduction in the photoelectric heating efficiency due to the destruction of the small dust grains and PAHs by strong AGN radiation fields. Our goal is to use the 24 μm emission as an SFR tracer; thus, we remove from our sample the AGN-selected regions in order to avoid non-star-forming contributions to the emission.

Figure 2, right panel, shows the $\Sigma_{24 \mu\text{m}} - \Sigma_{[\text{C II}]}$ correlation after removing the [C II] 3σ upper limits and the AGN points.

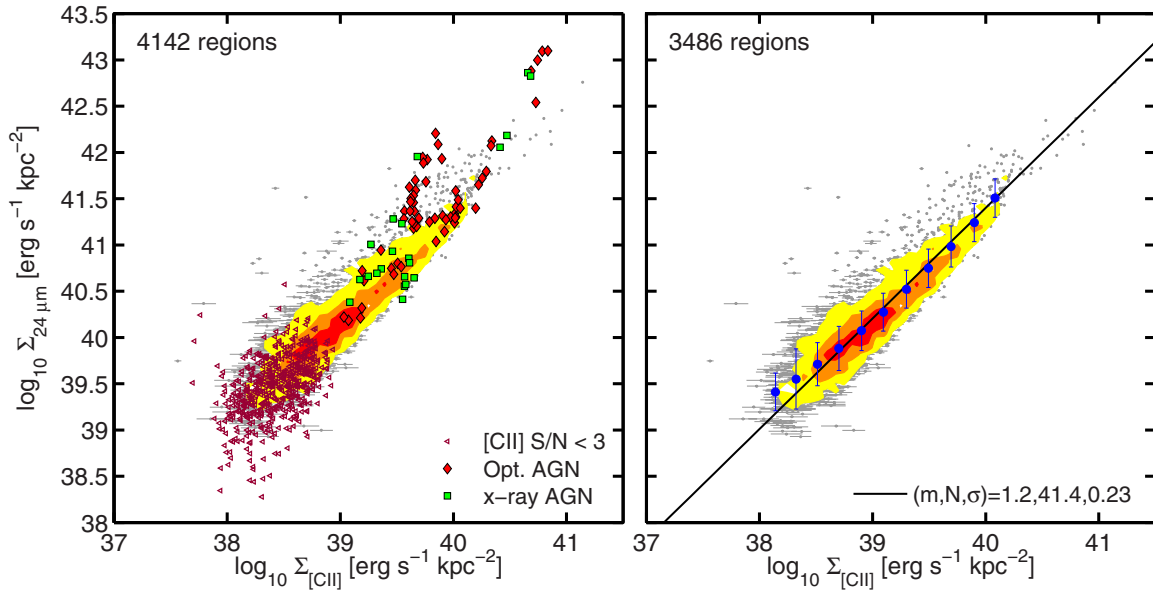


Figure 2. $24\ \mu\text{m}$ surface brightness ($\Sigma_{24\ \mu\text{m}}$) vs. $[\text{C II}]$ $158\ \mu\text{m}$ surface brightness ($\Sigma_{[\text{C II}]}$) of 46 galaxies from the KINGFISH sample. Filled contours show the data density (similar to a Hess diagram), and enclose 90%, 45%, and 25% of the data. Left: triangles correspond to $[\text{C II}]$ 3σ upper limits of regions with $S/N < 3$ ($\sim 11\%$ of the points). The diamonds and squares represent the regions located within the central ~ 0.5 kpc radius in 25 galaxies classified as AGNs ($\sim 2\%$ of the points). Regions from the 19 galaxies optically classified as AGNs are shown as red diamonds. Regions from the six galaxies that, based on the nuclear X-ray luminosity may indicate AGN activity, are shown as green squares. Right: same as the left panel, but excluding points with $[\text{C II}]$ $S/N < 3$, with emission associated with AGNs. The black line corresponds to the best linear fit to the data (in the log–log space). The slope, the logarithmic value of $\Sigma_{24\ \mu\text{m}}$ at $\log_{10}(\Sigma_{[\text{C II}]}/(\text{erg s}^{-1} \text{ kpc}^{-2})) = 40$, and the standard deviation dex of the fit are listed as (m, N, σ) on the bottom right corner. The blue dots show the running median and standard deviation in bins of $\Sigma_{[\text{C II}]}$.

The black solid line represents the best linear fit to the remaining 3486 points and the blue points show the median $\Sigma_{24\ \mu\text{m}}$ in bins of $\Sigma_{[\text{C II}]}$ with error bars indicating 1σ scatter. The correlation is tight, with a 1σ scatter around the fit of 0.23 dex and a slope of 1.20 ± 0.01 . This value is in excellent agreement with the 1.23 slope found by Calzetti et al. (2007) for the $\Sigma_{24\ \mu\text{m}} - \Sigma_{\text{SFR}}$ correlation; thus, we expect a nearly linear correlation between $\Sigma_{[\text{C II}]}$ and Σ_{SFR} . We discuss more about the $\Sigma_{[\text{C II}]} - \Sigma_{\text{SFR}}$ relationship in Section 4.

3.1.2. $24\ \mu\text{m}$ “Cirrus” Emission

Emission at $24\ \mu\text{m}$ can be used as a reliable obscured SFR tracer (Calzetti et al. 2007; Rieke et al. 2009); an important consideration, however, is to account for the $24\ \mu\text{m}$ emission that is produced by dust heated by non-star-forming sources (e.g., old stars). We will refer to this emission as $24\ \mu\text{m}$ cirrus.

We estimate the intensity of the $24\ \mu\text{m}$ cirrus following a similar procedure to the one described in Leroy et al. (2012). The details of the cirrus calculation are presented in Appendix C. The challenge in this method is to quantify the incident radiation field produced by non-star-forming sources, i.e., U_{cirrus} . For our estimation of the $24\ \mu\text{m}$ cirrus emission, we assume two distinct scenarios: (1) U_{cirrus} is constant across the galaxy, or (2) U_{cirrus} scales with U_{min} (in the DL07 model, U_{min} corresponds to the least interstellar radiation field heating the diffuse ISM). The resulting fraction of the $24\ \mu\text{m}$ emission associated with cirrus (f_{cir}) and the effect of the cirrus correction on the $\Sigma_{24\ \mu\text{m}} - \Sigma_{[\text{C II}]}$ correlation can be found in Table 1. In summary, $24\ \mu\text{m}$ cirrus corrections based on a scaled version of U_{min} do not produce significant changes on the $\Sigma_{[\text{C II}]} - \Sigma_{24\ \mu\text{m}}$ correlation, and the fraction of $24\ \mu\text{m}$ cirrus emission is, on average, in the 18%–39% range (depending on the scaling factor assumed). We conclude that the results are robust to the choice of correction except when the correction is pushed to extreme values (e.g.,

Description	Slope m	Normalization ^a N	Scatter (1σ dex)	r_{corr}	Median $f_{\text{cir}}(-1\sigma, +1\sigma)$
No cirrus	1.20	41.40	0.23	0.92	0 (0, 0)
Scaled cirrus					
$U_{\text{cir}} = 0.5 U_{\text{min}}$	1.21	41.32	0.24	0.89	0.18 (0.12, 0.24)
$\dots = 0.75 U_{\text{min}}$	1.27	41.32	0.24	0.89	0.29 (0.19, 0.39)
$\dots = U_{\text{min}}$	1.30	41.26	0.27	0.87	0.39 (0.28, 0.51)
Constant cirrus					
$U_{\text{cir}} = 0.6$	1.30	41.41	0.24	0.90	0.15 (0.06, 0.25)
$\dots = 0.8$	1.38	41.43	0.26	0.90	0.26 (0.11, 0.42)
$\dots = 1.1$	1.60	41.50	0.33	0.87	0.43 (0.20, 0.66)

Note. ^a The normalization N is the value of $\log_{10}(\Sigma_{24\ \mu\text{m}})$ at $\log_{10}(\Sigma_{[\text{C II}]} = 40$. Units are $\text{erg s}^{-1} \text{ kpc}^{-2}$.

$U_{\text{cirrus}} = 1.1$). We know these extreme and likely fairly drastic cirrus assumptions are not representative of our local, ~ 1 kpc neighborhood. Therefore, for the rest of the paper we choose to work with the $24\ \mu\text{m}$ cirrus subtraction that is based on the same assumption made by Leroy et al. (2012) for their sample of local galaxies, i.e., $U_{\text{cirrus}} = 0.5 U_{\text{min}}$.

3.2. $[\text{C II}]$ Compared to Other Star Formation Tracers: $H\alpha$, FUV, and $24\ \mu\text{m}$

On average, interstellar dust absorbs roughly half the starlight of typical spiral galaxies and re-emits it in the infrared; therefore, observations in the infrared are essential for deriving a complete inventory of star formation (Kennicutt & Evans 2012). The best way to account for this dust-driven extinction is to combine unobscured star formation tracers, like $H\alpha$ or FUV emission, with the dust-reprocessed infrared continuum. In this section we explore the correlations between $[\text{C II}]$ and the SFR estimated

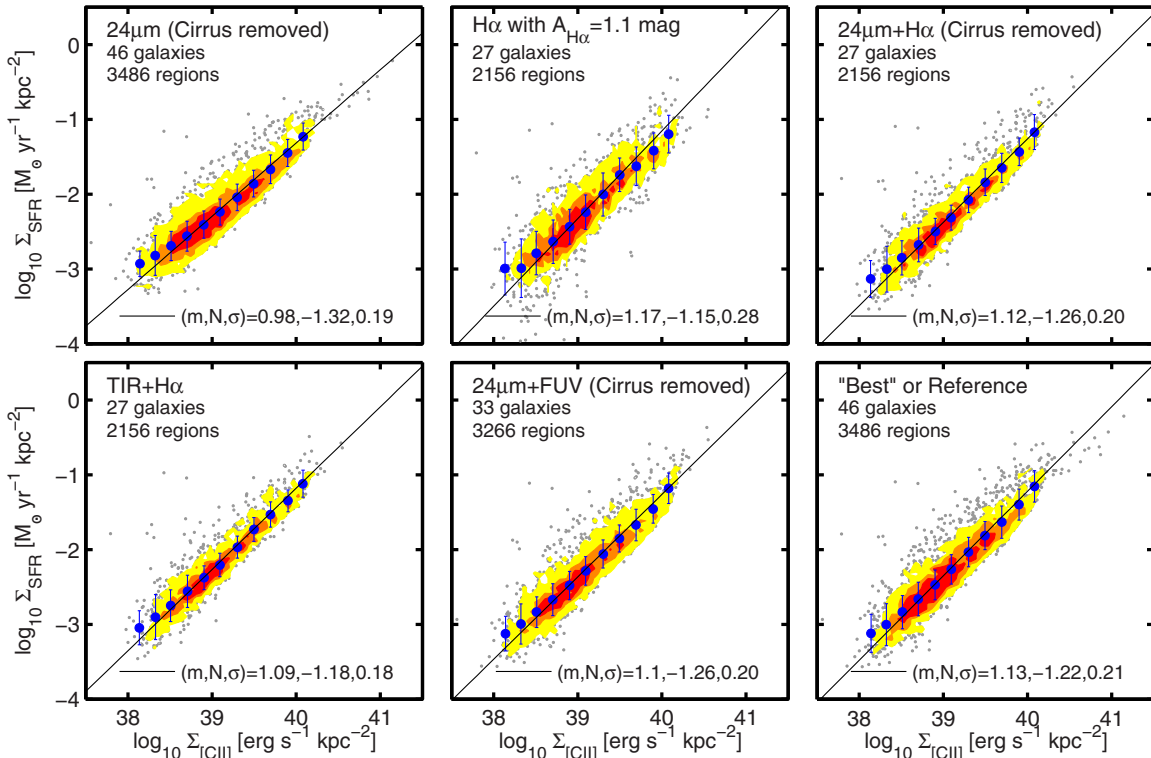


Figure 3. Star formation rate surface density, Σ_{SFR} , vs. $[\text{C II}]$ $158\ \mu\text{m}$ surface brightness, $\Sigma_{[\text{C II}]}$, for 46 galaxies from the KINGFISH sample. Gray points correspond to $12''$ (1 beam) size regions and filled contours show data density. The numbers on the bottom right corner of each panel correspond to the fit parameters: slope (m), y -axis value at $x = 40$ (N), and 1σ standard deviation in dex (σ). Each panel shows the correlation for a different method of measuring Σ_{SFR} . Top left: we measure Σ_{SFR} from $24\ \mu\text{m}$ emission (after cirrus subtraction) following Calzetti et al. (2007) calibration. Top middle: for 27 galaxies with $\text{H}\alpha$ maps available, we measure Σ_{SFR} from $\text{H}\alpha$ emission, corrected for internal extinction (1.1 mag), following Calzetti et al. (2007) calibration. Top right: we estimate Σ_{SFR} based on the combination of $24\ \mu\text{m}$ emission (cirrus subtracted) and $\text{H}\alpha$ emission for the 27 galaxies for which $\text{H}\alpha$ maps are available. We use Calzetti et al. (2007) calibration. Bottom left: we measure Σ_{SFR} from the combination between TIR and $\text{H}\alpha$ emission following Kennicutt et al. (2009) calibration. Bottom middle: we measure Σ_{SFR} as the combination of $24\ \mu\text{m}$ emission (cirrus subtracted) and FUV emission for 33 galaxies with FUV maps available following Leroy et al. (2008) calibration. Bottom right: we show the “Best” or Reference Σ_{SFR} , which we measure from $\text{H}\alpha+24\ \mu\text{m}$ (when $\text{H}\alpha$ is available), FUV+ $24\ \mu\text{m}$ (when $\text{H}\alpha$ is not available), and only $24\ \mu\text{m}$ when neither $\text{H}\alpha$ nor FUV maps are available.

from $24\ \mu\text{m}$ and TIR emission and combinations of $24\ \mu\text{m}$ and TIR with $\text{H}\alpha$ and FUV emission.

We measure the SFR and Σ_{SFR} based on (1) $\text{H}\alpha$ emission using Calzetti et al. (2007) calculation, Equation (6), and applying a typical extinction correction of $A_{\text{H}\alpha} = 1.1\ \text{mag}$ (Kennicutt 1983). Calzetti et al. (2007) adopts the default *Starburst99* initial mass function (IMF), i.e., a truncated Salpeter IMF with slope 1.3 in the range $0.1\text{--}0.5\ M_{\odot}$ and slope 2.3 in the range $0.5\text{--}120\ M_{\odot}$. (2) $24\ \mu\text{m}$ emission using Equations (8) and (9) in Calzetti et al. (2007). (3) The combination of $24\ \mu\text{m}$ and $\text{H}\alpha$ using Calzetti et al.’s (2007) calculation, Equation (7). (4) The combination of TIR luminosity and $\text{H}\alpha$ using Kennicutt et al. (2009) Equation (16) and a scaling coefficient of 0.0024 (Table 4, Kennicutt et al. 2009). As Calzetti et al. (2007), Kennicutt et al. (2009) also adopts the default *Starburst99* IMF. We measure the TIR emission using 8, 24, 70, and $160\ \mu\text{m}$ bands following Equation (22) in Draine & Li (2007). (5) The combination of $24\ \mu\text{m}$ and FUV, using Leroy et al. (2008) Equations (D10) and (D11). These two calibrations were constructed from the FUV-based SFR calibration by Salim et al. (2007). For all galaxies the $24\ \mu\text{m}$ continuum emission is cirrus subtracted following Section 3.1.2.

Figure 3 shows the correlations we find between $\Sigma_{[\text{C II}]}$ and Σ_{SFR} . The first panel shows the correlation for 46 galaxies for which we measure Σ_{SFR} using only $24\ \mu\text{m}$ emission. The slope of the correlation is nearly linear and the scatter is 0.19 dex.

The next panel shows Σ_{SFR} measured using $\text{H}\alpha$ for the 27 galaxies for which we have $\text{H}\alpha$ data available. The correlation is good ($r_{\text{corr}} = 0.83$), with the highest surface brightness points lying below the main trend probably because of increasing extinction in $\text{H}\alpha$. Given that $\text{H}\alpha$ is a tracer of recent star formation, with an age sensitivity of a few Myr (McKee & Williams 1997), the fact that we find a good correlation with $[\text{C II}]$ strengthens the case in favor of using this FIR cooling line as an SFR tracer. For the same 27 galaxies, the third and fourth panels show the combination between $\text{H}\alpha$ and $24\ \mu\text{m}$ and TIR emission, respectively. Combining $\text{H}\alpha$ and IR continuum emission significantly reduces the scatter and corrects for the attenuation of $\text{H}\alpha$ emission at high SFR values. The fifth panel shows the $\Sigma_{[\text{C II}]} - \Sigma_{\text{SFR}}$ correlation for 33 galaxies when using a combination of $24\ \mu\text{m}$ and FUV emission to measure Σ_{SFR} . The correlation is tight, with a 1σ scatter around the fit of 0.2 dex. The fit parameters are similar to those measured when the SFR is measured as a combination of $\text{H}\alpha$ and $24\ \mu\text{m}$ emission.

Given that we do not have $\text{H}\alpha$ or FUV maps available for all the galaxies in our sample, unlike $24\ \mu\text{m}$, we define the Σ_{SFR} we use from now on as “our reference” Σ_{SFR} coming from the combination of (1) $24\ \mu\text{m} + \text{H}\alpha$ (27 cases); (2) $24\ \mu\text{m} + \text{FUV}$ if $\text{H}\alpha$ is not available (8 cases); (3) only $24\ \mu\text{m}$ if neither $\text{H}\alpha$ nor FUV are available (11 cases). The correlation between the $\Sigma_{[\text{C II}]}$ and “our reference” Σ_{SFR} is shown in the last panel of Figure 3. The best linear fit to the data, as estimated by the

ordinary least-squares (OLS) linear bisector method (Isobe et al. 1990), yields the following relationship:

$$\Sigma_{\text{SFR}}(M_{\odot} \text{ yr}^{-1} \text{ kpc}^{-2}) = 3.823 \times 10^{-47} \times (\Sigma_{[\text{C II}]}(\text{erg s}^{-1} \text{ kpc}^{-2}))^{1.130}. \quad (2)$$

The scatter of the correlation is 0.21 dex.

In order to derive a calibration for the SFR based on [C II] luminosities, we convert the [C II] luminosity surface densities into [C II] luminosities, and then we fit the data using the OLS linear bisector method. The resulting [C II]-based SFR calibration is

$$\text{SFR}(M_{\odot} \text{ yr}^{-1}) = 2.286 \times 10^{-43} \times (L_{[\text{C II}]}(\text{erg s}^{-1}))^{1.034}. \quad (3)$$

The scatter of the correlation is 0.21 dex. Due to the distance effect introduced by the conversion to luminosities, the calibration in Equation (3) has a slope closer to unity, but similar scatter. Recall that “luminosity–luminosity” relations implicitly have distance squared in both axes ($\propto D^2$), while in “surface density–surface density” correlations, the quantities in both axes depend upon the ratio between luminosity ($\propto D^2$) and area ($\propto D^2$), so surface densities are independent of distance.

Before applying these calibrations, it is important to understand their reliability and limits of applicability. For instance, the luminosity calibration is subject to the caveats mentioned in the Introduction regarding the “[C II]-deficit,” which implies that galaxies with similar IR luminosity can show variations of a factor of 10× or more in their [C II] luminosity (Stacey et al. 2010). In order to explore the reliability of the [C II]–SFR calibration, in the next section we study in detail the nature of the scatter in the [C II]–SFR correlation and we also apply these calibrations to other samples of extragalactic objects observed in [C II] emission.

4. ANALYSIS

In the previous section we found a tight correlation between $\Sigma_{[\text{C II}]}$ and Σ_{SFR} . In this section we try to understand the origin of this correlation and the reason why some galaxies or regions within galaxies deviate from this quasi-linear relationship.

Variations of the [C II] luminosity compared to the IR continuum were first observed by *ISO*. Low [C II] to FIR ratios are found for global measurements of normal star-forming galaxies with warm dust temperatures ($F_{\nu}(60 \mu\text{m})/F_{\nu}(100 \mu\text{m}) \gtrsim 0.8$; Malhotra et al. 1997, 2001; Brauher et al. 2008) and U/LIRGs ($L_{\text{IR}} > 10^{11-12} L_{\odot}$; Luhman et al. 1998, 2003). This is important in the context of our study because the FIR luminosity is commonly used as an SFR tracer in U/LIRGs. Therefore, any variation in the [C II] to FIR ratio will imply a difference between the SFR measured using [C II] and FIR emission.

With *Herschel*, low [C II] to FIR ratios are observed for U/LIRGs as a function of increasing dust temperature, compactness of the source (Díaz-Santos et al. 2013) and FIR luminosity to molecular gas mass (M_{H_2}) ratio (Graciá-Carpio et al. 2011). In addition, *Herschel* allowed for the first time to resolve the regions that exhibit low [C II] to FIR ratios in nearby galaxies. Croxall et al. (2012) observe in NGC 4559 and NGC 1097 a drop in the [C II] to FIR ratio for regions with warm dust temperatures ($\nu f_{\nu}(70 \mu\text{m})/\nu f_{\nu}(100 \mu\text{m}) \gtrsim 0.95$) and intense radiation fields. They conclude that the most plausible scenario to account for the [C II] deficit is the charging of the dust grains caused by the high radiation fields. Beirão et al. (2012) find a

similar trend when comparing the circumnuclear ring and extranuclear regions of NGC 1097.

Similar to the observed variations in the [C II] to FIR ratios, De Looze et al. (2014) report variations in the [C II] to SFR correlation observed in galaxies from the DGS sample. Compared to a standard SFR measured as a combination of FUV and 24 μm emission, they find systematically lower values of [C II]-based SFRs as a function of increasing dust temperature, [O I] 63 μm /[C II] + [O I] 63 μm ratio, and decreasing metallicity. Thus, for warm, low-metallicity regions De Looze et al. (2014) conclude that [O I] 63 μm is a more reliable SFR tracer than [C II]. For additional discussion on the connection between metal abundance and the dispersion of the [C II]–SFR correlation, see De Looze et al. (2014).

In order to evaluate the reliability of an SFR calibration based on the [C II] line, it is key to understand the scatter in the correlation. The goal is to identify the variables that drive the deviations from the fit (Equations (2) and (3)), and use this information to reduce the scatter and establish the limits of applicability of the calibration. In the next two sections we discuss how local regions within a galaxy and galaxies as a whole deviate from the fit. We study the deviations as a function of a set of parameters that characterize the ISM properties and can be derived directly from the dust continuum spectral energy distributions (SEDs) and spectra. These parameters are (1) IR color, $\nu f_{\nu}(70 \mu\text{m})/\nu f_{\nu}(160 \mu\text{m})$; (2) oxygen abundance ($12 + \log(\text{O}/\text{H})$); (3) fraction of the IR luminosity radiated from regions with high radiation fields, $f(L_{\text{IR}}; U > 100)$; (4) dust-weighted mean starlight intensity, $\langle U \rangle$; and (5) PAH abundance, q_{PAH} . These last three parameters are derived from the DL07 dust model (see Appendix B for details).

4.1. Local Variations

The high spatial resolution provided by *Herschel* allow us to study the scatter on \sim kiloparsec scales. The benefit of studying local variations in a large sample of galaxies with varying global properties is that it allow us to identify the more likely of the possible scenarios behind the scatter. Figure 4 summarizes the results of our fit residual analysis for all the $\sim 12''$ regions of the 46 galaxies in our sample. The top left panel shows the fit residual as a function of IR color, which is an observable quantity and can be used as a proxy for the dust temperature. About 20% of the regions have IR colors warmer than $\nu f_{\nu}(70 \mu\text{m})/\nu f_{\nu}(160 \mu\text{m}) \gtrsim 1.3$; the fit residual for these regions systematically increases as a function of IR color, with a median deviation from the fit as high as a factor of ~ 3 for the warmest regions (i.e., warm dust regions systematically exhibit higher Σ_{SFR} (or SFR) than expected from their [C II] meaning they are underluminous in [C II]). This corresponds to a particular dust color temperature, T_{dust} . We estimate T_{dust} using a modified blackbody model with emissivity spectral index $\beta = 1.5$ and the 70–160 μm flux ratio. Most of the regions have dust color temperatures in the range $T_{\text{dust}} \sim 20\text{--}32$ K, and we find that regions start to systematically deviate from the fit for dust color temperatures higher than $T_{\text{dust}} \gtrsim 29$ K.

A similar trend is observed as a function of the model-derived variables. The remaining left panels of Figure 4 show that for a dust-weighted mean starlight intensity of $\langle U \rangle \gtrsim 6$, a fraction of the IR luminosity produced in high radiation field regions $f(L_{\text{IR}}; U > 100) \gtrsim 25\%$, or a PAH abundance $q_{\text{PAH}} \lesssim 2\%$, points tend to deviate from the fit in a similar fashion as for IR color. It is important to note that $\sim 99\%$, $\sim 85\%$, and $\sim 73\%$ of the regions with $\langle U \rangle \gtrsim 6$, $f(L_{\text{IR}}; U > 100) \gtrsim 25\%$, and $q_{\text{PAH}} \lesssim 2\%$

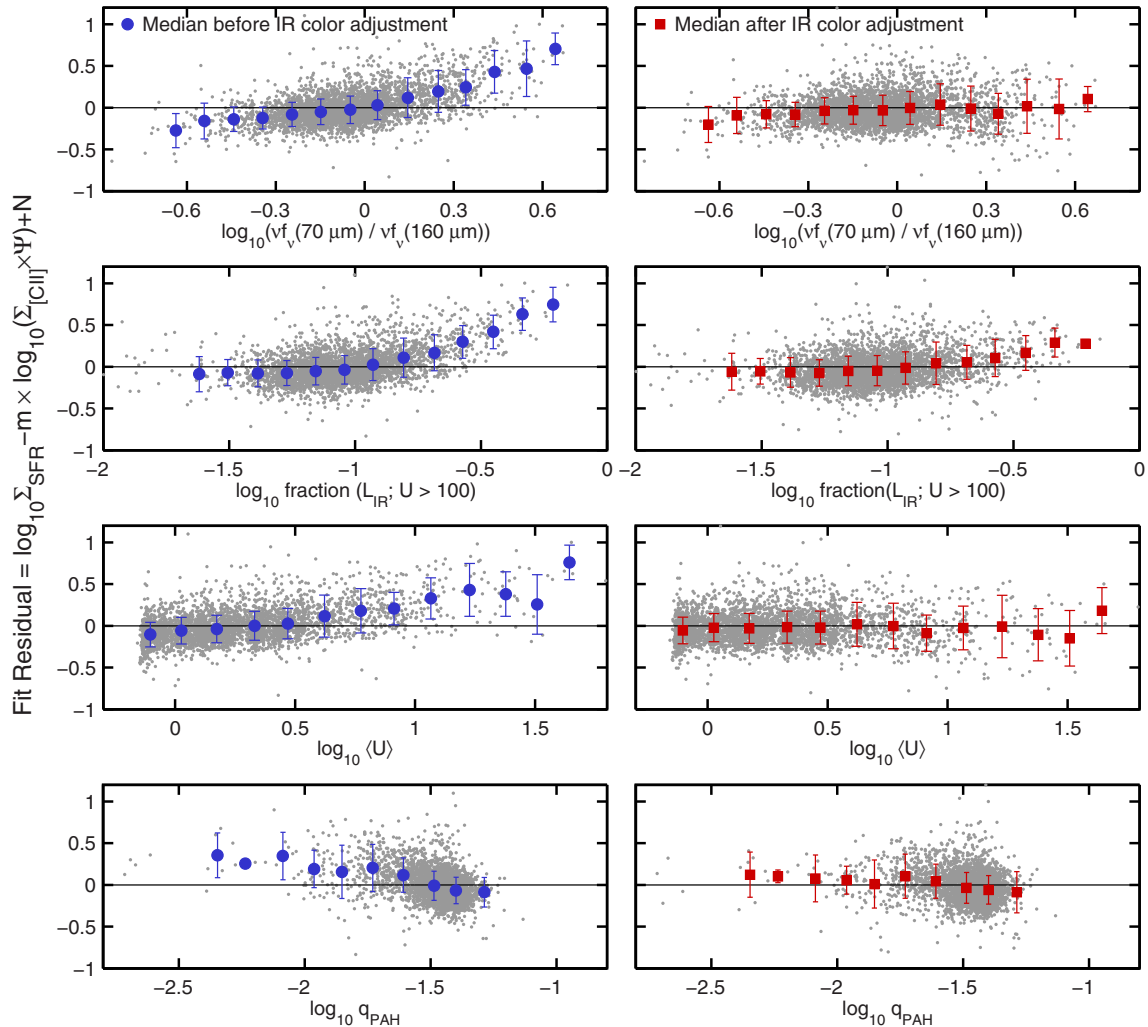


Figure 4. Fit residual of the $\Sigma_{\text{CII}} - \Sigma_{\text{SFR}}$ correlation as a function of IR color (ν_{70}/ν_{160}), fraction of the IR luminosity radiated from regions with high radiation field ($\text{fraction}(L_{\text{IR}}; U > 100)$), median radiation field ($\langle U \rangle$), and PAH abundance (q_{PAH}). The left and the right panel show the fit residual before and after applying the IR color adjustment derived in Section 4.2.1, respectively. Gray points represent $12''$ size regions of the 46 galaxies in the sample. Filled blue dots (left panel), red squares (right panel), and the corresponding vertical bars correspond to the median and the 1σ standard deviation in dex of the binned distribution of points.

have IR colors $\gtrsim 1.3$, respectively; this shows that regions that systematically deviate from the fit in the different panels are essentially the same. We also observed a similar systematic deviation as a function of the ν_{70}/ν_{100} IR color, starting at the threshold value of $\nu_{70}/\nu_{100} \approx 0.8$.

We also analyze the local variations as a function of dust attenuation, which we measure as the fraction of FUV and optical emission absorbed and reprocessed by dust versus the escaping FUV emission as the ratio of the $24\mu\text{m}$ to the FUV intensity, $I_{24\mu\text{m}}/I_{\text{FUV}}$. The details of this analysis can be found in Appendix D. Around the $I_{24\mu\text{m}}/I_{\text{FUV}}$ ratio of ~ 10 , we observe a systematic increase of the fit residuals as a function of decreasing dust attenuation. low-metallicity regions from Holmberg II and IC 2574 also show high fit residuals at low $I_{24\mu\text{m}}/I_{\text{FUV}}$ ratios, and we discuss the implications of these results in Section 4.2.1.

Before analyzing the possible physical reasons behind the fit residual increase described in the previous paragraph, we need to discard the possibility that these deviations are not introduced by systematic disagreements between the different SFR tracers combined to produce our reference Σ_{SFR} (Section 3.2). In order to explore this possibility, we first construct two alternative

versions of the reference Σ_{SFR} : one that is solely based on the combination of $24\mu\text{m}$ and $\text{H}\alpha$, and one that is based on the combination of $24\mu\text{m}$ and FUV only. For both cases, we observe a similar systematic increase of the fit residuals as a function of $\langle U \rangle$ as the one shown in Figure 4. Therefore, we discard the possibility that the way we construct our reference Σ_{SFR} has any implication on the observed trend of the fit residuals.

Next, we try to identify the physical basis for the systematic increase of the fit residuals. As we mentioned before, at least $\sim 85\%$ of the regions with warm IR colors ($\gtrsim 1.3$) show evidence of high radiation fields. These regions also show lower PAH abundances, which is expected given that it appears that PAHs are destroyed in H II regions (Povich et al. 2007). One of the possible reasons for the systematic increase of the residual toward positive values is the decrease of the photoelectric heating efficiency due to the positive charging of the dust grains and the decrease in the gas heating rates due the lower abundance of PAHs. What this implies for the purpose of measuring the Σ_{SFR} (or SFR) based on Σ_{CII} (or L_{CII}) alone is that a simple calibration that ignores dust color temperature will underestimate the amount of star formation activity in these regions.

Table 2
IR Color Adjustment Coefficients

$\log_{10}(\Sigma_{\text{SFR}}) = m \times \log_{10}(\Sigma_{[\text{C II}]} \times \Psi(\gamma)) + N$		
IR Color (γ)	Threshold (γ_t)	α
$\nu f_\nu(70 \mu\text{m})/\nu f_\nu(160 \mu\text{m})$	1.24	0.94
$\nu f_\nu(70 \mu\text{m})/\nu f_\nu(100 \mu\text{m})$	0.80	1.57
$\log_{10}(\text{SFR}) = m \times \log_{10}(L_{[\text{C II}]} \times \Psi(\gamma)) + N$		
IR Color (γ)	Threshold (γ_t)	α
$\nu f_\nu(70 \mu\text{m})/\nu f_\nu(160 \mu\text{m})$	1.12	1.20
$\nu f_\nu(70 \mu\text{m})/\nu f_\nu(100 \mu\text{m})$	0.80	1.90

Note. Coefficients m and N can be found in Table 3.

4.1.1. IR Color Adjustment

Motivated by the observed systematic increase of the fit residual after a given IR color threshold, we derived an IR color adjustment that accounts for the underestimation of Σ_{SFR} (or SFR). We choose an adjustment based on an IR color, over a model-dependent variable adjustment (e.g., $\langle U \rangle$) because the IR color is observable, free of assumptions, and easier to measure. For a given IR color $\gamma(\lambda_1, \lambda_2) = \nu f_\nu(\lambda_1 \mu\text{m})/\nu f_\nu(\lambda_2 \mu\text{m})$, we define the IR color factor Ψ as

$$\Psi(\gamma) = \begin{cases} 1 & \text{if } \gamma < \gamma_t \\ (\gamma/\gamma_t)^\alpha & \text{if } \gamma \geq \gamma_t. \end{cases} \quad (4)$$

The IR color threshold, γ_t , and the power-law exponent, α , are derived in order to minimize the logarithmic residuals between the observed and the [C II]-based Σ_{SFR} (or SFR). Values of γ_t and α for the IR colors $\gamma(70, 100)$ and $\gamma(70, 160)$ are listed in Table 2. This proposed IR color based adjustment Ψ represents a simple and straightforward attempt to account for the systematic increment of the fit residual of regions that show warm colors/high radiation fields. Based on the IR color factor Ψ , the adjusted [C II] surface brightness (or luminosity) can now be written as $\Sigma_{[\text{C II}]} \times \Psi$ (or $L_{[\text{C II}]} \times \Psi$).

The effects of the IR color adjustment on the correlation residuals are shown in the right panels of Figure 4. The red squares show the adjusted median residuals as a function of IR color, $\langle U \rangle$, $f(L_{\text{IR}}; U > 100)$, and q_{PAH} . By design, the IR color adjustment removes the trend of increasing residuals with IR color for warmer regions. This is true even for the last bin in IR color where the difference between the adjusted and the unadjusted data is a factor of ~ 3 . As the second and third left panels show, applying the IR color adjustment also helps to remove the trend of increasing residuals with $\langle U \rangle$ and $f(L_{\text{IR}}; U > 100)$. This is a consequence of the large overlap between regions with warm colors and high radiation field signatures. In the case of the PAH abundance, the fourth panel shows that the IR color adjustment helps to reduce the increasing residuals as a function of q_{PAH} . This is expected given the correlation between IR color, $\langle U \rangle$ and q_{PAH} .

4.2. Galaxy-to-galaxy Variations

In this section we continue the study of the scatter of the correlation, but this time in terms of the galaxy-to-galaxy variations. Treating each galaxy as a single point is an oversimplification of the underlying physics, but it is useful because frequently only a global measurement of the [C II] flux can be obtained.

In order to analyze how much each galaxy deviates from the fit as a whole, we fix the slope to that determined for

the $\Sigma_{[\text{C II}]} - \Sigma_{\text{SFR}}$ correlation (i.e., 1.13 ± 0.01 , Equation (2)) and then we calculate the median residual for each galaxy. Figure 5 shows the median fit residual as a function of IR color ($\nu f_\nu(70)/\nu f_\nu(160)$), dust-weighted mean starlight intensity ($\langle U \rangle$), fraction of the IR luminosity radiated from regions with high radiation fields, $f(L_{\text{IR}}; U > 100)$, and the global measurements of oxygen abundance ($12 + \log_{10}(\text{O}/\text{H})$). Each point represents one galaxy. Those with mean IR colors below the IR color adjustment threshold (i.e., $\gamma_t(70, 160) = 1.24$) are shown as filled circles. The rest of the galaxies, for which the IR color adjustment applies, are shown as filled and open squares for unadjusted and adjusted mean residual values, respectively.

The first panel of Figure 5 shows the median residuals as a function of IR color. Starting around $\nu f_\nu(70)/\nu f_\nu(160) \sim 1.2$, we observe a trend of increasing residuals with warmer IR color, similar to what we find in the analysis for the resolved regions (Section 4.1). The effect of the IR color adjustment on the residuals is clearly shown by the growing separation between the unadjusted and adjusted mean residual values as a function of IR color. The second and the third panels show the residual as a function of two radiation field strength related parameters: $\langle U \rangle$ and $f(L_{\text{IR}}; U > 100)$. We find that systems with $\langle U \rangle \gtrsim 3$ or $f(L_{\text{IR}}; U > 100) \gtrsim 20\%$ start to show increasing deviations from the fit. This is similar to what we observe in the IR color panel and expected given the close connection between the radiation field strength and the IR color. As we previously showed in the analysis of the resolved regions, it is clear from these two panels how the IR color adjustment helps to reduce the absolute scatter in the correlation. In terms of the standard deviation of the median residuals, applying the IR color adjustment reduces the galaxy-to-galaxy scatter from 0.22 dex to 0.16 dex.

4.2.1. Low-metallicity Galaxies

The KINGFISH sample contains only a handful of low-metallicity systems, which despite their paucity show some potentially interesting trends. The bottom panel in Figure 5 shows that low-metallicity galaxies tend to deviate from the fit. What this implies for the three of them—Holmberg II, IC 2574, and NGC 5408—is that the [C II]-based calibration yields an SFR that is at least a factor of ~ 4 lower than the SFR measured using the standard tracers available (i.e., FUV+24 μm for Holmberg II and IC 2574, and 24 μm for NGC 5408). These are diffuse galaxies with no well-defined bulge or nucleus, so we discard potential AGN contamination in the SFR measurement (Moustakas et al. 2010). In the case of the irregular dwarf galaxy IC 2574, the [C II] data covers only the H I supergiant shell located in the northeast part of the galaxy discovered by Walter et al. (1998). This region contains a central stellar cluster about 11 Myr old and recent star formation activity located in the rim of the expanding shell (Stewart & Walter 2000). This FUV intense environment heats the surrounding dust grains, resulting in high dust temperatures. In fact, this region from IC 2574, Holmberg II, and NGC 5408 correspond to the three warmest systems in our sample as measured by their IR colors: for an emissivity index of $\beta = 1.5$, their dust color temperatures are in the $T_{\text{dust}} = 30\text{--}34$ K range. In addition, these galaxies have [C II] to TIR luminosity ratios in the 0.35%–0.6% range. This is slightly higher than the 0.3% measured for the Milky Way (Wright et al. 1991). Compared to other low-metallicity systems, these ratios are lower than those found for NGC 4214 (0.5%–0.8%; Cormier et al. 2010) and the Large Magellanic Cloud (0.9%; Rubin et al. 2009), and higher than those measured

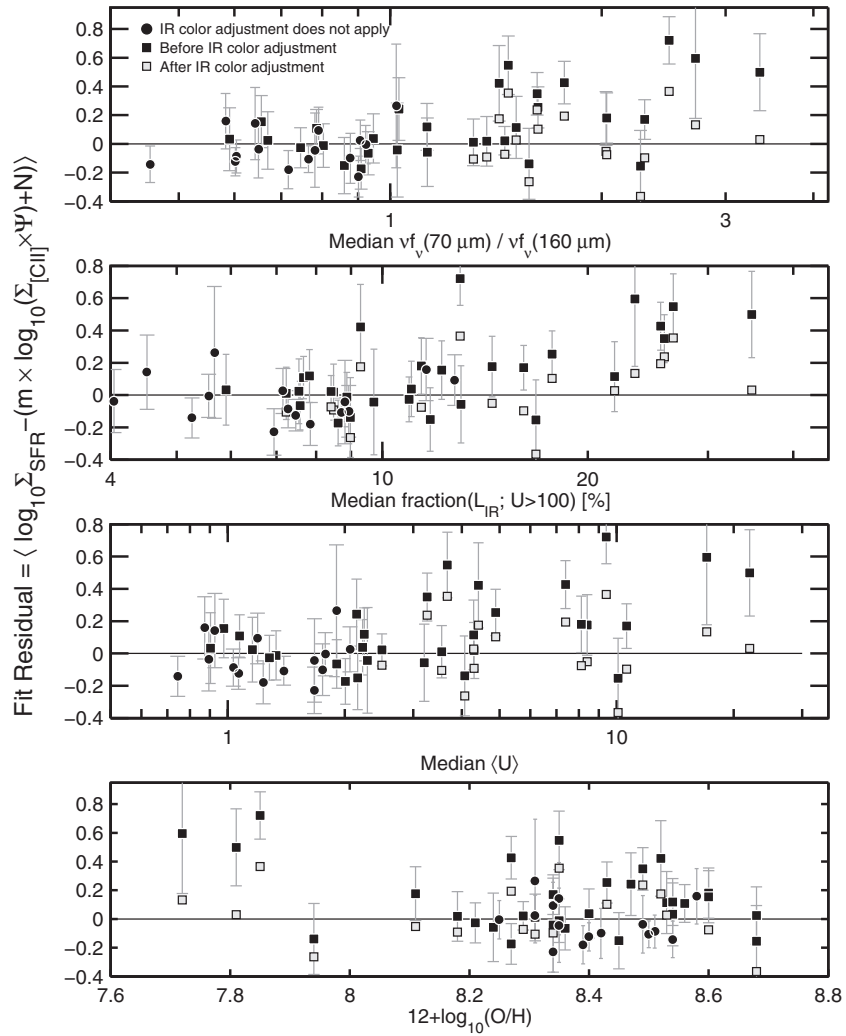


Figure 5. Median of the fit residual for each of the 46 galaxies in our sample vs. median IR color ($v_f(70 \mu\text{m})/v_f(160 \mu\text{m})$), median radiation field ($\langle U \rangle$), median fraction of the luminosity coming from regions with $U > 100$ and oxygen abundance ($12 + \log_{10}(\text{O}/\text{H})$). The vertical bars represent 1σ standard deviation around the median. Black squares and open squares show the median fit residual before and after applying the IR color adjustment. Black circles show the median fit residual for galaxies that, on average, are not warm enough to apply the IR color adjustment.

in 30 Doradus (0.12%; Poglitsch et al. 1995) and Haro 11 (0.1%; Cormier et al. 2012).

There are multiple factors that can play a role in the high $\Sigma_{\text{SFR}}/\Sigma_{\text{SFR}([\text{C II}]})$ ratios observed in low-metallicity regions (e.g., De Looze et al. 2014). If we assume that it is correct to use the same method to measure Σ_{SFR} in both high- and low-metallicity regions, then the high residuals can only be explained by variations in the heating and [C II] cooling as a function of metallicity. On one hand in low-metallicity environments, low PAH abundances, low dust-to-gas ratios, and low FUV extinction reduce the gas heating efficiency and heating rate. On the other, FUV photons produced by O and B stars travel farther from their point of origin, thereby producing a low diffuse FUV flux in much of the ISM that may keep dust grains mostly electrically neutral and maintain a high gas heating efficiency (Israel & Maloney 2011). Note, however, that we measure the highest dust temperatures, implying high dust-weighted mean starlight intensities ($\langle U \rangle > 10$), in our low-metallicity sample.

A possible explanation of the deviations observed in low-metallicity regions is that we are missing a non-negligible fraction of the neutral gas cooling, coming out in FIR lines other than [C II] (e.g., [O I] $63 \mu\text{m}$). In order to explore this scenario, we measure the ratio of the [O I] $63 \mu\text{m}$ to [C II] emission as

a function of the SFR surface density. Figure 6 shows the line ratio for 962 regions in the KINGFISH sample for which we have [O I] $63 \mu\text{m}$ and [C II] detections with $S/N > 3$. At low Σ_{SFR} values, regions tend to have higher [O I] $63 \mu\text{m}$ to [C II] line ratios compared to the rest of the sample. To investigate this, we have done data simulations in which we apply different S/N cuts, and we find that the absence of regions with small line ratios at low Σ_{SFR} is not real, but most likely a bias introduced by the selection of the $S/N = 3$ cut. From Figure 6 we conclude that the [O I] $63 \mu\text{m}$ line emission is not the dominant cooling channel for the KINGFISH metal-rich regions. We also include in the plot the three low-metallicity systems in our sample: NGC 5408 (blue) and 3σ upper limits for Holmberg II (red) and IC 2574 (magenta). Together with these low-metallicity regions, the other regions in our sample that show Σ_{SFR} to $\Sigma_{\text{SFR}([\text{C II}]})$ ratios greater than two are shown as circles with gray borders. It can be seen that these regions tend to show higher [O I] $63 \mu\text{m}$ to [C II] line ratios than the rest of the sample. In the case of NGC 5408, the cooling of the neutral gas is approximately equally split between the [C II] and [O I] $63 \mu\text{m}$ transitions. This result is similar to the [C II] to [O I] $63 \mu\text{m}$ ratios of 1.1 and 1.2 measured by Hunter et al. (2001) for the irregular galaxies NGC 1569 and IC 4662, respectively. For Holmberg II and IC 2574, the

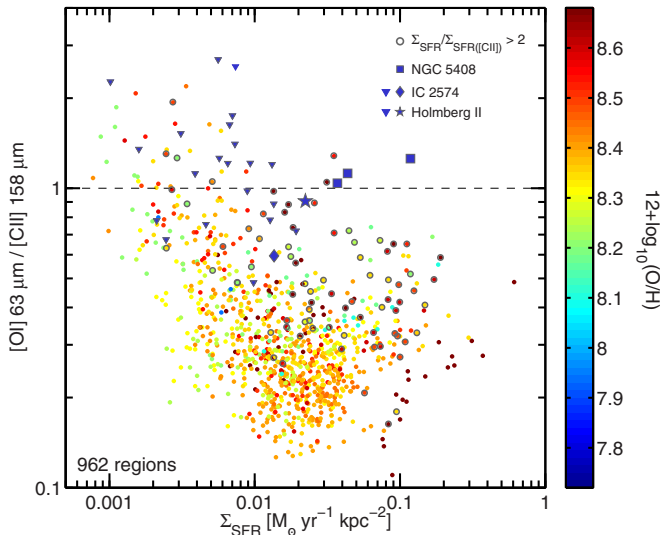


Figure 6. Ratio between the [O I] 63 μm and [C II] 158 μm emission for regions selected from the KINGFISH sample as a function of the SFR surface density (Σ_{SFR}) measured as the combination of 24 μm , H α , and FUV emission (see Section 3.2). The color scale shows the global metallicity value of the galaxy from Moustakas et al. (2010). The circles with gray borders show regions where this Σ_{SFR} value is greater than the [C II]-based Σ_{SFR} by more than a factor of two. The panel also shows regions selected from three low-metallicity systems: Holmberg II (star), IC 2574 (diamond), and NGC 5408 (square). The triangles pointing down correspond to 3σ upper limits due to non-detections in [O I] 63 μm emission. These low-metallicity regions also tend to show [C II]-based Σ_{SFR} values that are lower than Σ_{SFR} by a factor of two or more (see Figure 5, panel 4).

upper limits do not rule out the possibility of a non-negligible contribution to the cooling of the neutral gas via [O I] 63 μm . What this implies for low-metallicity regions is that a purely [C II]-based SFR calibration would underestimate the total SFR value; for NGC 5408, this would account for at least half of the factor of ~ 4 deviation.

Can [O I] 63 μm emission be used to provide a better SFR estimate? De Looze et al. (2014) find that a [C II]-based SFR calibration systematically underestimates the SFR as a function of increasing [O I] 63 μm /[C II] + [O I] 63 μm ratio. For regions with sub-solar metallicity, they conclude that [O I] 63 μm is a more reliable SFR tracer than [C II] emission. Over the same KINGFISH sample we study in [C II], the $\Sigma_{[\text{O I}]} - \Sigma_{\text{SFR}}$ correlation has a slope of 1.2 and a scatter of 0.25 dex. This is less linear and has higher scatter than what we measure in the $\Sigma_{[\text{C II}]} - \Sigma_{\text{SFR}}$ correlation. It is possible that the sample of dwarf galaxies in De Looze et al. (2014) is biased toward starbursting systems, where stronger radiation fields arising from dense PDRs favor [O I] as a more reliable star formation tracer than [C II]. If we combine the [C II] and [O I] 63 μm emission in our sample, we find that the slope and the scatter of the correlation between $\Sigma_{[\text{C II}] + [\text{O I}]} - \Sigma_{\text{SFR}}$ are similar to that of the $\Sigma_{[\text{C II}]} - \Sigma_{\text{SFR}}$ correlation.

Perhaps more importantly, at lower metallicities we expect lower dust optical depth, resulting in regions that are more transparent to the FUV radiation than their metal-rich counterparts because of low dust-to-gas ratios. Under these conditions, the fraction of FUV photons that escapes the system without interactions with the dust is larger than at normal metallicity. In dense PDRs—the main source of [O I] emission—the FUV leakage would play against the production of both lines, [C II] and [O I], for which interaction of FUV photons with the dust is required for heating. We speculate, however, that the lower

density material that emits preferentially in [C II] is more affected by the escape of FUV photons, giving rise to higher [O I] 63 μm /[C II] ratios in these sources. This would help to explain the high [O I] 63 μm /[C II] ratios observed in the low-metallicity regions compared to the rest of the sample.

A higher fraction of escaping FUV photons at low metallicity would also imply that the IR emission would not be able to account for the total value of the SFR. As an example, Calzetti et al. (2007) find that using 24 μm emission can underestimate the SFR of low-metallicity systems by a factor of ~ 2 –4. In order to explore this scenario we measure the FUV to [C II] and FUV to TIR ratios, which can be used as a rough measure of the amount of extinction at ultraviolet wavelengths (Dale et al. 2007). We find that the mean FUV to [C II] ratio (and the corresponding 68% range in parenthesis) for the low-metallicity regions from Holmberg II and IC 2574 is 281(134–588), whereas the remaining 31 galaxies with FUV data available have a median FUV to [C II] ratio of 32(13–77). We observe a similar trend for the FUV to TIR ratios. Thus our results favor the scenario described above, where a larger fraction of escaping FUV photons in low-metallicity regions would mostly explain the low SFRs based on [C II] emission.

4.2.2. Dependence of the Correlation Fit Parameters with Distance and Inclination

The galaxies in our sample span a range in distance (2.8–26.5 Mpc) and inclination ($\lesssim 75^\circ$) that might have potential consequences on the individual $\Sigma_{[\text{C II}]} - \Sigma_{\text{SFR}}$ correlation properties. To test this, we look for trends between the correlation fit parameters and the distance or inclination of the source. We fit the $\Sigma_{[\text{C II}]} - \Sigma_{\text{SFR}}$ correlation for each individual galaxy using the OLS bisector method (we leave out of this analysis four galaxies that have fewer than five pointings with $S/N > 3$). We do not find any clear trend between the fit parameters (i.e., slope and normalization) with distance or inclination. The Pearson correlation coefficient for the four correlations made as the combination of the slope/normalization versus the distance/inclination is less than ~ 0.2 for all the cases. Therefore we conclude that the calibrations presented here are robust to spatial resolution and inclination.

4.3. The [C II] – Star Formation Rate Correlation Before and After the IR Color Adjustment

As we show in Sections 4.1 and 4.2, it is possible to use an IR color based adjustment to reduce the scatter of both the $\Sigma_{\text{SFR}} - \Sigma_{[\text{C II}]}$ and $\text{SFR} - L_{[\text{C II}]}$ correlations. The consequences of applying these adjustments are shown in Figure 7. The left panel shows the $\Sigma_{[\text{C II}]} - \Sigma_{\text{SFR}}$ correlation before applying the IR color adjustment. The regions that are warm enough to be modified by the adjustment ($\nu f_\nu(70)/\nu f_\nu(160) \geq 1.25$) are shown as blue dots. The black solid line corresponds to the best fit to the data (Equation (2)). The right panel on Figure 7 shows the correlation after applying the IR color adjustment. The net effect is that the asymmetry of the scatter cloud decreases, reducing the dispersion of the correlation to 0.19 dex. The OLS bisector fit to the IR color corrected correlation $\Sigma_{[\text{C II}]}$ yields a slope that is slightly closer to linear (1.08).

Table 3 summarizes the best-fit parameters we measure for the $\Sigma_{\text{SFR}} - \Sigma_{[\text{C II}]}$ and $\text{SFR} - L_{[\text{C II}]}$ correlations. We also list the 1σ dispersion around the fit and the correlation coefficient r_{corr} . We include the calibration coefficients for four different cases: (1) the correlation including the 24 μm normal cirrus subtraction. These correspond to the coefficients in Equation (2)

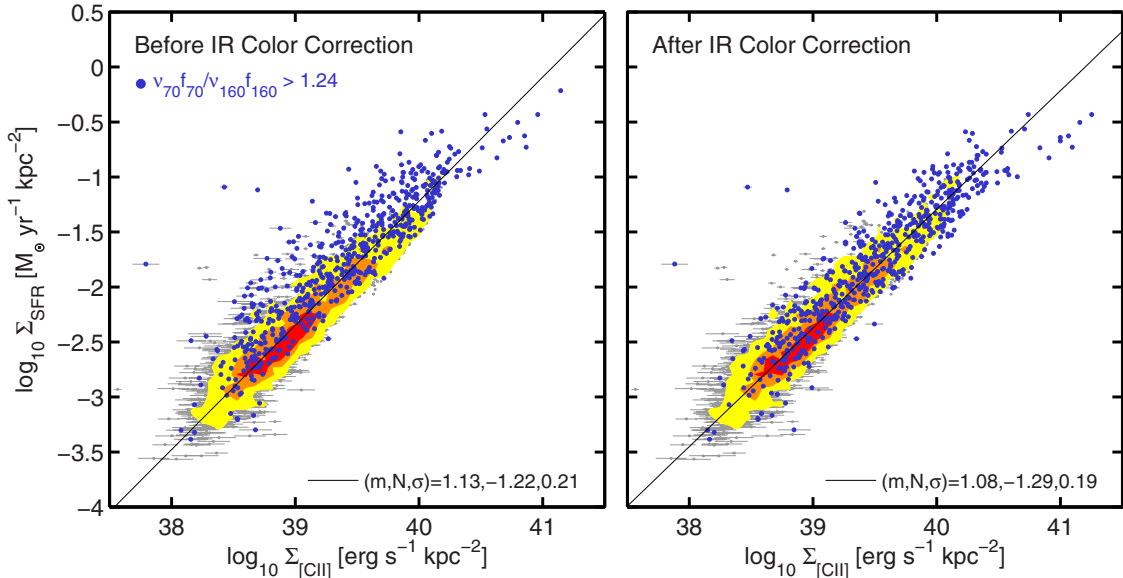


Figure 7. Left: star formation rate surface density, Σ_{SFR} , as a function of [C II] $158 \mu\text{m}$ surface brightness, $\Sigma_{[\text{C II}]}$, for 46 galaxies from the KINGFISH sample. Σ_{SFR} is estimated from $\text{H}\alpha+24 \mu\text{m}$ (when $\text{H}\alpha$ is available), FUV+ $24 \mu\text{m}$ (when $\text{H}\alpha$ is not available), and only $24 \mu\text{m}$ when neither $\text{H}\alpha$ nor FUV maps are available. Gray points correspond to $12''$ (1 beam) size regions and contours show data density. The numbers on the bottom right corner of each panel correspond to the fit parameters: slope (m), y -axis value at $x = 40$ (N), and 1σ standard deviation (σ). Right: same as the left panel, but for this case we adjusted the $\Sigma_{[\text{C II}]}$ using the IR color adjustment described in Equation (4).

Table 3
[C II]–SFR Calibration Coefficients and Uncertainties

$\log_{10}(\Sigma_{\text{SFR}}/(M_{\odot} \text{ yr}^{-1} \text{ kpc}^{-2})) = m \times (\log_{10}(\Sigma_{[\text{C II}]}/(\text{erg s}^{-1} \text{ kpc}^{-2})) - 40) + N$				
Description	Slope m	Normalization ^a N	Scatter (1σ dex)	r_{corr}
Normal $24 \mu\text{m}$ cirrus (Equation (2))	1.130 ± 0.007	-1.217 ± 0.008	0.21	0.92
IR color adjusted	1.079 ± 0.007	-1.296 ± 0.008	0.19	0.93
Strong $24 \mu\text{m}$ cirrus	1.182 ± 0.009	-1.249 ± 0.010	0.23	0.90
Fixed slope	1.000	-1.342 ± 0.010	0.21	0.92
$\log_{10}(\text{SFR}/(M_{\odot} \text{ yr}^{-1})) = m \times (\log_{10}(L_{[\text{C II}]}/(\text{erg s}^{-1})) - 40) + N$				
Description	Slope m	Normalization ^b N	Scatter (1σ dex)	r_{corr}
Normal $24 \mu\text{m}$ cirrus (Equation (3))	1.034 ± 0.008	-1.281 ± 0.010	0.22	0.94
IR color adjusted	0.977 ± 0.005	-1.401 ± 0.008	0.20	0.96
Strong $24 \mu\text{m}$ cirrus	1.031 ± 0.007	-1.357 ± 0.011	0.24	0.92
Fixed slope	1.000	-1.328 ± 0.010	0.22	0.94

Notes.

^a The normalization N is the value of $\log_{10}(\Sigma_{\text{SFR}}/(M_{\odot} \text{ yr}^{-1} \text{ kpc}^{-2}))$ at $\log_{10}(\Sigma_{[\text{C II}]}/(\text{erg s}^{-1} \text{ kpc}^{-2})) = 40$.

^b The normalization N is the value of $\log_{10}(\text{SFR}/(M_{\odot} \text{ yr}^{-1}))$ at $\log_{10}(L_{[\text{C II}]}/(\text{erg s}^{-1})) = 40$.

and Equation (3); (2) same as (1), but after applying the IR color adjustment from Equation (4); (3) the correlation after applying the strong $24 \mu\text{m}$ cirrus subtraction (which assumes $U_{\text{cirrus}} = U_{\text{min}}$); (4) if we fit the correlation using a fixed slope of 1. For regions or galaxies in the surface brightness range of the KINGFISH sample ($10^{39} \lesssim \Sigma_{[\text{C II}]} \lesssim 10^{40.5}$ ($\text{erg s}^{-1} \text{ kpc}^{-2}$)), the resulting SFRs using the calibration parameters from the first two cases are very similar. However, the calibration coefficients from case 1 (Equations (2) and (3)) seem better suited to measure SFRs in higher surface brightness objects (e.g., LIRGs) as can be seen in the next section.

As a summary, the [C II]-based calibration can be written as

$$\log_{10}(\Sigma_{\text{SFR}}) = m \times (\log_{10}(\Sigma_{[\text{C II}]} \times \Psi(\gamma)) - 40) + N, \quad (5)$$

where the calibration coefficients m and N are listed in Table 3. We recommend using the calibration coefficients from

Equation (2). If there is IR color information available, we also recommend using Table 2 to measure the IR color factor Ψ and apply the IR color adjustment to the [C II] emission.

5. COMPARISON WITH MODELS AND OBSERVATIONS

5.1. Comparison with Other Extragalactic [C II] Samples

Comparing our results with previous analyses done for samples of galaxies observed in [C II] by *ISO* and *Herschel* can provide useful information about the reliability and limits of applicability of our [C II]-based SFR calibration. This is particularly true for very luminous galaxies, which are poorly represented in the KINGFISH sample. This comparison can be done in surface density or luminosity space. Surface density comparisons are the most interesting from a physical standpoint, since they are distance independent. Moreover, surface density

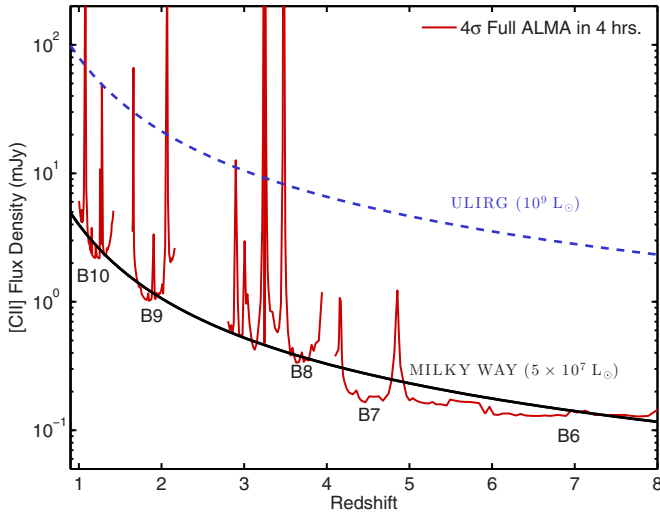


Figure 8. ALMA’s ability to detect Milky-Way-type (black line at $5 \times 10^7 L_{\odot}$; Wright et al. 1991; Bennett et al. 1994) and ultraluminous-infrared-type galaxies (dashed blue line at $10^9 L_{\odot}$) in the [C II] $158 \mu\text{m}$ transition after four hours of time integration as a function of redshift. The red line represents ALMA’s sensitivity estimated using the ALMA sensitivity calculator (assuming a linewidth of 300 km s^{-1}). From Band 10 (B10) to Band 6 (B6), galaxies can be detected by ALMA in the [C II] transition in the redshift range of $z \sim 1.2\text{--}7$.

is more directly related to parameters like radiation field intensity, which are thought to dominate the physical processes in PDRs. Luminosity, on the other hand, is frequently the only measurement directly available for very distant galaxies, and it is thus also interesting to investigate. For instance, Figure 8 shows ALMA’s ability to detect, in the [C II] transition, galaxies like the Milky Way and ULIRGs as a function of redshift. For an integration time of four hours, the full ALMA can potentially detect in the [C II] transition Milky-Way-type galaxies at redshift intervals that span the range from $z \sim 1.2$ to 7.

First, we perform the comparison in the surface density space. For this purpose, we use galaxies from the Great Observatories All-sky LIRG Survey (GOALS; Armus et al. 2009). A brief description of the selection criteria and properties of the GOALS systems included in this analysis is available in Appendix D. Figure 9 shows the $\Sigma_{\text{SFR}} - \Sigma_{[\text{C II}]}$ correlation for the KINGFISH regions and the GOALS galaxies; the latter are divided into pure starburst with $L_{\text{FIR}} < 10^{11} L_{\odot}$ and non-AGN U/LIRGs. The left and right panels show the correlation before and after applying the IR color adjustment, respectively. The solid line in both panels represents Equation (2). The dashed line correspond to the best linear fit to the KINGFISH regions (Table 3). For the data with no IR color adjustment applied, the GOALS pure starburst galaxies with $L_{\text{FIR}} < 10^{11} L_{\odot}$ and $\Sigma_{[\text{C II}]} \lesssim 10^{41.5} (\text{erg s}^{-1} \text{ kpc}^{-2})$ agree well with Equation (2). At greater luminosity surface densities, these systems start to systematically deviate from the fit, although they still lie roughly within a factor of two from Equation (2). On the other hand, all the non-AGN U/LIRGs lie above the fit, following a trend parallel to the KINGFISH data. If we fit the GOALS pure starburst with $L_{\text{FIR}} < 10^{11} L_{\odot}$ and non-AGN U/LIRGs using the slope from Equation (2), we find that the fit normalization is, on average, a factor of 1.5 and 3 higher, respectively. When compared to the linear fit, GOALS starbursts galaxies with $\Sigma_{[\text{C II}]} \gtrsim 10^{41} (\text{erg s}^{-1} \text{ kpc}^{-2})$ show deviations in the $\sim 5\text{--}10$ range. As we show in Section 4.1, part of these deviations are associated with the IR color of the region. Therefore, we apply the IR adjustment derived for

the KINGFISH sample to the regions and galaxies in both samples. The right panel in Figure 9 shows the IR-color-adjusted correlation, where the good agreement between the KINGFISH and the GOALS samples with Equation (2) across nearly five orders of magnitude in $\Sigma_{[\text{C II}]}$ and Σ_{SFR} is evident. On the other hand, the linear [C II]-based calibration—even after applying the IR color adjustment—continue to underestimate the reference Σ_{SFR} value.

Next, we perform the comparison in luminosity space. In addition to the galaxies from the GOALS sample, we include in the analysis galaxies used by Boselli et al. (2002), De Looze et al. (2011), and Sargsyan et al. (2012) to derive their [C II]-based SFR calibrations. We also include non-AGN, non-merger LIRGs from B. Weiner et al. (in preparation). The general properties of these additional samples of galaxies are described in Appendix D. In order to compare our KINGFISH results to the other samples, we re-derive their published SFRs and TIR luminosities, so we can ensure uniformity and comparability to our work.

The results of the comparison between the KINGFISH galaxies and the samples described above are shown in Figure 10. The two panels show the ratio of the [C II]-based SFR calibration (Equation (3)) to the SFR measured using standard tracers as a function of TIR luminosity. Each black point corresponds to the mean SFR of a KINGFISH galaxy, and the vertical bars represent the 1σ standard deviation around the mean value. The TIR luminosity of the KINGFISH galaxies was measured over the area covered by the [C II] observations and not the entire system. The left panel shows the galaxies before applying the IR color adjustment. We see that the largest deviations occur at both TIR luminosity ends. At $L_{\text{TIR}} \lesssim 10^9 L_{\odot}$, six out of the eight systems that show deviations larger than a factor of ~ 3 have metallicities below $12 + \log_{10}(\text{O}/\text{H}) \lesssim 8.2$: Holmberg II and IC 2574 from the KINGFISH sample; NGC 625, NGC 1569, and NGC 1156 from the De Looze et al. (2011) sample; and IC 4662 from the Boselli et al. (2002) sample. The remaining two galaxies, NGC 4698 and NGC 4429 from the Boselli et al. (2002) sample, do not have metallicity measurements available. At the high TIR luminosity end, the SFR measured using the [C II]-SFR calibration underestimates the SFR(TIR) value for almost all the LIRGs. The non-AGN LIRGs show deviations that can be as high as a factor of ~ 10 . If we fit these systems using the slope from Equation (3), we find that the fit normalization is, on average, a factor of 4.4 ± 1.9 higher. Similarly, De Looze et al. (2014) find that in the $L_{[\text{C II}]} - \text{SFR}$ plane, ULIRGs tend to be offset from starburst and AGNs by a factor between 3 and ~ 10 . These deviations are a direct consequence of the significant scatter in the [C II] to TIR ratio observed in U/LIRGs (Malhotra et al. 1997, 2001; Braucher et al. 2008; Díaz-Santos et al. 2013). It is important to mention, however, that monochromatic IR-based SFR tracers (e.g., $24 \mu\text{m}$) agree much better with the SFR inferred from [C II] through our calibration; but integrated indicators such as TIR are usually considered better measures of the SFR in U/LIRGs.

The right panel shows the result of applying the IR color adjustment derived in our study. As shown in Section 4.1, the IR color adjustment helps to reduce the discrepancy for the low-metallicity KINGFISH galaxies; this is also true for the low-metallicity systems from the other samples. For the LIRGs, the IR color adjustment proves to have an important effect by reducing the difference between the SFR([C II]) and SFR(TIR) values to less than a factor of two for more than half of the systems. The IR color adjustment is especially effective with the

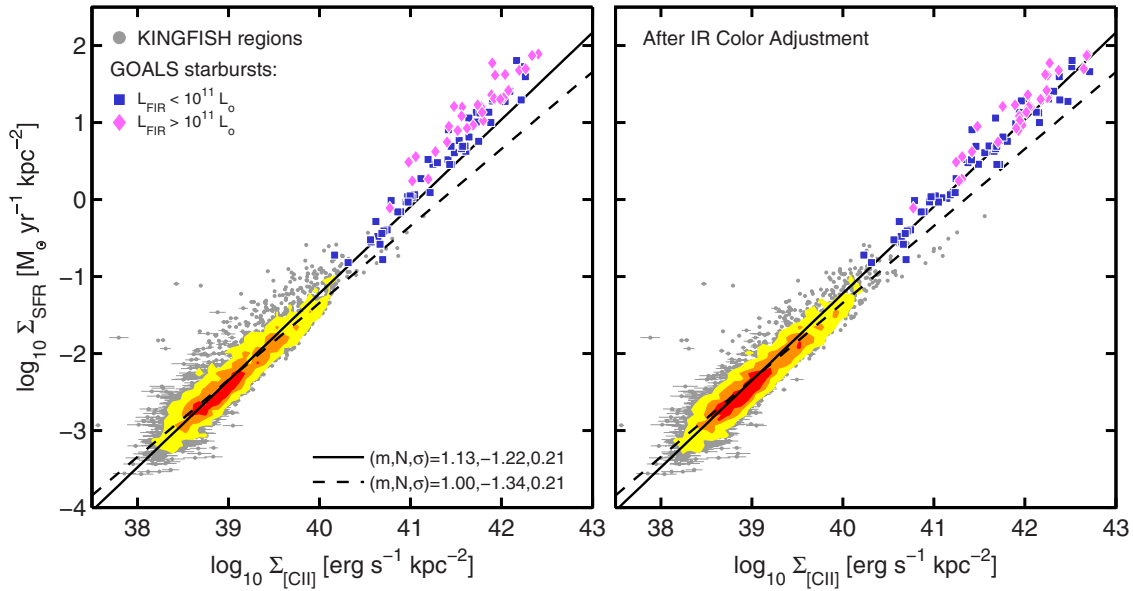


Figure 9. Left: star formation rate surface density vs. [C II] surface brightness for resolved regions from the KINGFISH sample (gray points and color density contours) and global measurements from a subset of pure starburst systems from the Great Observatories All-sky LIRG Survey (GOALS) sample. These were selected using their $6.2 \mu\text{m}$ PAH EW. The blue squares and the magenta diamonds show the GOALS galaxies that have IR luminosities lower and higher than $10^{11} L_{\odot}$, respectively. The solid and the dashed line correspond to Equation (2) and the fit with a fixed slope of 1, respectively. The numbers on the bottom right corner correspond to the fit parameters: slope (m), y -axis value at $x = 40$ (N), and 1σ standard deviation in dex (σ). These are the same parameters as in Equation (2). Right: same as the left panel, but for this case we adjusted the $\Sigma_{[\text{C II}]}$ in both samples using the IR color adjustment described in Equation (4). The solid and dashed lines are the same as in the left panel.

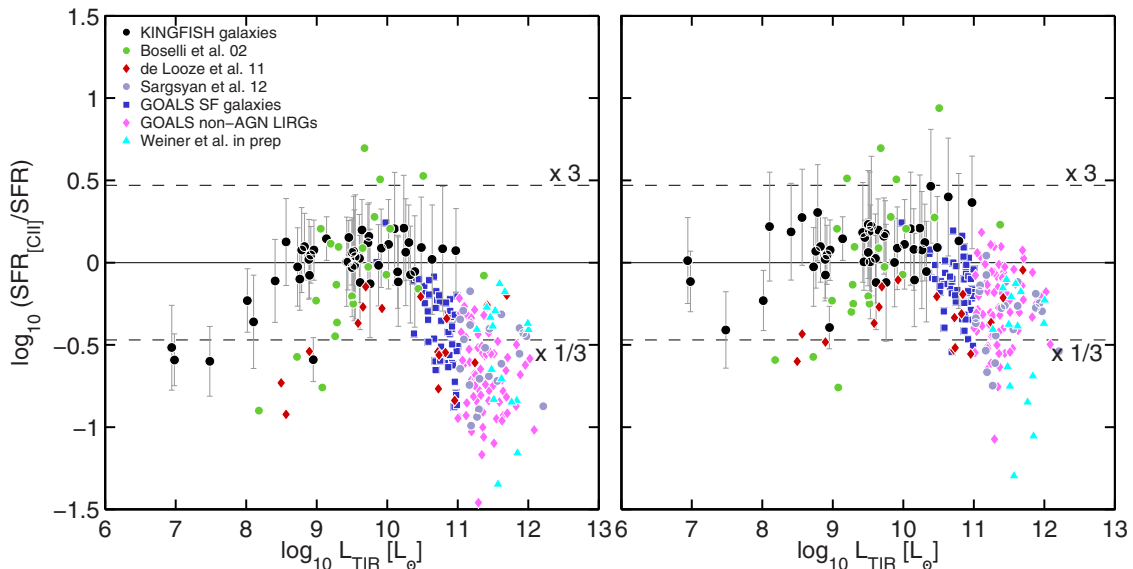


Figure 10. Ratio of the SFR measured using this work [C II] calibration (Equation (3)) to the SFR measured based on tracers other than [C II]. We treat each KINGFISH galaxy as an individual point (black circle) by taking the median value of the SFR and the sum of the TIR luminosity of all the regions in the galaxy that were observed in [C II]. The vertical bar represents the 1σ standard deviation around the SFR median. The other galaxy global measurements correspond to Boselli et al. 2002 (green circles), De Looze et al. 2011 (red diamonds), Sargsyan et al. 2012 (purple circles), Díaz-Santos et al. (2013) (blue squares and magenta diamonds), and B. Weiner et al. (in preparation; cyan circles). The left and right panels show the data before and after applying the IR color adjustment.

$L_{\text{IR}} < 10^{11} L_{\odot}$ pure starbursts from the GOALS sample. The LIRGs of the Sargsyan et al. (2012) sample, however, are not corrected enough to bring them into good agreement with the calibration. It is possible that the IR color of these galaxies is redder than the color of the regions from which most of the [C II] arises, or maybe a the color adjustment—although adequate for the KINGFISH sample—is too mild for many of these systems. If we fit all the LIRGs using the same slope as Equation (3), we find that the fit normalization is a factor of 1.9 higher. That is, the LIRGs can be placed on a relation approximately parallel to our calibration for normal galaxies, but displaced toward higher

SFR per [C II] emission. Note, however, that there is a large scatter of the U/LIRGs around this offset.

In summary, for samples of normal, star-forming galaxies and non-AGN LIRGs, the SFR measured using our [C II]–SFR calibration—after applying IR color adjustment—agrees within a factor of ~ 3 with the SFR from standard SFR tracers ($H\alpha$, FUV, $24 \mu\text{m}$, and FIR) for at least $\sim 80\%$ of the systems. The remaining galaxies can exhibit deviations as high as a factor of ~ 10 , showing the limitations of using the [C II] luminosities to measure SFRs in IR luminous and ultra-luminous systems. This is not the case for the $\Sigma_{[\text{C II}]} - \Sigma_{\text{SFR}}$ correlation, where

the KINGFISH regions and the GOALS starbursts agree within a factor of ~ 2 with the calibration (Equation (2)) over five orders of magnitude in $\Sigma_{[\text{C II}]}$. This calibration is more physically motivated than the luminosity one, because surface densities are connected to the radiation field strength, which has a strong influence on the drivers of the [C II] emission process. In the luminosity case, the same [C II] luminosity can be attained by a combination of high/low [C II] surface brightness over a small/large emitting area. The physical conditions in these two scenarios are significantly different, resulting in large deviations from the calibration for a given fixed [C II] luminosity.

5.2. Comparison with Models: Starburst99

In regions where the cooling is dominated by [C II] emission, we expect the FUV heating and the [C II] cooling to be closely related through the photoelectric effect in PAHs and small dust grains. In this section we explore this connection using a simple model based on the *Starburst99* code (Leitherer et al. 1999).

The first step in our calculation is to use *Starburst99* to model the luminosity of a stellar population for a constant SFR over 100 Myr. For the calculations we adopt the default evolutionary tracks, and assume a stellar population with solar metallicity. For the stellar IMF, we adopt the *Starburst99* default. The output of the model is the spectrum of a stellar population as a function of the duration of the star formation episode (t_d). From this spectrum, we measure the FUV luminosity by integrating over the FUV range of energy that dominates the grain photoelectric heating, i.e., $6 < E_\gamma < 13.6$ eV. Then, we scale the FUV luminosity by assuming a heating efficiency, ϵ_h , to estimate the amount of heating of the gas. ϵ_h is the product of two factors: (1) the photoelectric heating efficiency of the dust (ϵ_{ph}), that is mainly set by the ratio of the photoionization rate over the recombination rate of electrons with neutral grains/PAHs (Hollenbach & Tielens 1999; Weingartner & Draine 2001). Typical values for ϵ_{ph} are in the 0.1%–3% range; and (2) the fraction of the FUV photons in the $6 < E_\gamma < 13.6$ eV range that interact with dust and result in gas heating of the neutral and molecular ISM. We assume that the cooling of the gas is dominated by the [C II] transition, so for a given SFR, we connect the [C II] and FUV luminosities via $L_{[\text{C II}]} \sim \epsilon_h \times L_{\text{FUV}}(t_d)$ (as we show in Figure 6, this is a valid assumption for metal-rich regions).

Figure 11 shows the model results plotted on top of the $\Sigma_{[\text{C II}]} - \Sigma_{\text{SFR}}$ correlation. Each line represents a model output for a combination of t_d and ϵ_h . Dashed lines correspond to a population with a constant SFR and $t_d = 2$ Myr; the solid lines correspond to $t_d \geq 20$ Myr (because we are assuming a constant SFR scenario, the variation of the FUV luminosity in the 20–100 Myr range is less than $\sim 25\%$). As expected, for a given t_d and Σ_{SFR} , as ϵ_h increases, so does the predicted $\Sigma_{[\text{C II}]}$. Note that there is a degeneracy in the model between t_d and ϵ_h . For instance, the model output for the combination of input parameters $t_d = 2$ Myr and $\epsilon_h = 3\%$ is very similar to the model output when assuming $t_d \geq 20$ Myr and $\epsilon_h = 1\%$.

Figure 11 also shows individual star-forming regions (no IR color adjustment applied) selected from 46 KINGFISH galaxies. The data density contours represent the ensemble of all these regions. The bulk of the data can be explained as arising from regions that have been actively star-forming for $t_d > 20$ Myr, with ϵ_h in the 1%–3% range. This suggests that the scatter is mainly driven by changes in ϵ_h . On the other hand, to describe the bulk of the data assuming $t_d = 2$ Myr requires an unusually high heating efficiency of $\epsilon_h > 3\%$.

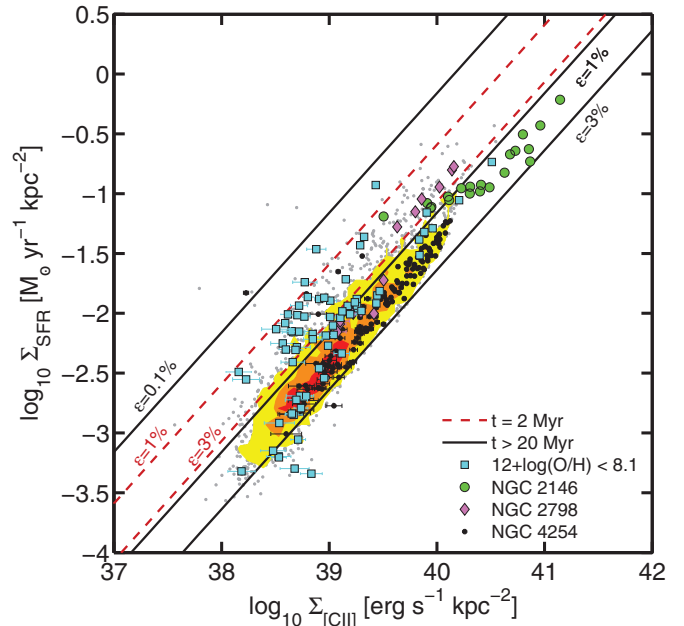


Figure 11. Star formation rate surface density vs. [C II] surface density (no IR color adjustment applied). The gray points and the corresponding data density contours show the star-forming regions selected from 48 galaxies of the KINGFISH sample. We also highlight individual galaxy cases: NGC 2146 (green circles), NGC 2798 (magenta diamonds), NGC 4254 (black circles), and regions from low-metallicity galaxies with $12 + \log(\text{O}/\text{H}) \lesssim 8.1$ (cyan squares). The diagonal lines represent the model output. We use *Starburst99* to model the FUV luminosity of a stellar population for a given SFR value and a constant star formation scenario. We then convert the FUV emission into a [C II] surface brightness by assuming a heating efficiency of ϵ_h . Thus, each diagonal line is the combination of a t_d Myr old population with constant star formation rate and ϵ_h . Dashed lines correspond to $t_d = 2$ Myr; the solid line correspond to $t_d \geq 20$ Myr.

The model suggests two possible explanations to describe the regions that deviate the most from the main trend and tend to lie in the upper side of the scatter cloud: (1) an early stage of the star formation episode ($t_d = 2$ Myr) and ϵ_h in the 1%–3% range, or (2) standard star formation duration of $t_d \geq 20$ Myr and low ϵ_h ($\lesssim 1\%$). The second scenario is widely applicable because it does not require fine tuning of the ages, and we know that at high UV fields small grains become positively charged or are destroyed, thus reducing ϵ_h .

Finally, Figure 11 highlights four individual cases. One of them, NGC 4254, is a spiral galaxy chosen to illustrate a system that follows the main trend. The other three are as follows.

NGC 2146. This system has the highest total IR luminosity in our sample, $L_{\text{TIR}} = 10^{11} L_\odot$, and can be classified as a LIRG. The regions from NGC 2146 have [C II] luminosity surface densities in the range $10^{40} \lesssim \Sigma_{[\text{C II}]} \lesssim 10^{41.3}$ ($\text{erg s}^{-1} \text{kpc}^{-2}$). The majority of them follow the main trend and can be described by heating efficiencies in the 1%–3% range and $t_d \geq 20$ Myr.

NGC 2798. About half of the regions of this galaxy show a higher ratio of Σ_{SFR} to $\Sigma_{[\text{C II}]}$ compared to the rest of the data. NGC 2798 is a barred spiral that is part of an interacting pair with NGC 2799. There is evidence from UV spectra for a recent burst of star formation (Joseph et al. 1986). This agrees well with the calculations for a duration of the star formation of about $t_d = 2$ Myr and ϵ_h in the range 1%–3%.

Galaxies with $12 + \log(\text{O}/\text{H}) < 8.1$. Here we select regions from four low-metallicity galaxies that have oxygen abundances $12 + \log(\text{O}/\text{H}) < 8.1$. These systems are: Holmberg II, IC 2574, NGC 2915, and NGC 5408 (Moustakas et al. 2010). As shown

in Figure 5, about half of the low-metallicity regions deviate from the fit, showing higher $\Sigma_{\text{SFR}}/\Sigma_{[\text{C II}]}$ ratios than the rest of the points. In these systems two scenarios are possible: (1) the regions are young and have been forming stars at a continuous rate for only $t_d = 2$ Myr, and the heating efficiency is in the $\epsilon_h \simeq 1\%–3\%$ range; or (2) the regions have been forming stars at a continuous rate for $t_d \geq 20$ Myr and the heating efficiency of the medium is lower than $\epsilon_h \sim 1\%$. As we concluded in Section 4.2.2, the deviations observed in low-metallicity regions are most likely described by the latter scenario, where a reduction in the heating efficiency is expected due to reduced trapping of FUV photons by the dust.

6. SUMMARY AND CONCLUSIONS

We study the [C II] 158 μm line emission and its potential to be used as a SFR tracer, using a set of nearby galaxies drawn from the *Herschel* KINGFISH sample. The [C II] surface brightness, $\Sigma_{[\text{C II}]}$, can be used as a robust Σ_{SFR} tracer in normal, star-forming galaxies in the absence of strong AGNs. In this work we present a calibration for that relation (Equation (2)) that is based on 3486 regions selected from 46 nearby galaxies. The uncertainty associated with the calibration is ± 0.21 dex. One of the main sources of scatter are regions with warm IR colors. We derive a set of adjustments based on the IR color factor Ψ (Equation (4) and Table 2) that helps to reduce the scatter among the warmer regions. Therefore, if the size of the object and two of the 70, 100 and 160 μm fluxes are available, we recommend measuring the SFR surface density using the IR-color-adjusted version of Equation (2):

$$\Sigma_{\text{SFR}}(M_{\odot} \text{ yr}^{-1} \text{ kpc}^{-2}) = 3.823 \times 10^{-47} \times (\Sigma_{[\text{C II}]}(\text{erg s}^{-1} \text{ kpc}^{-2}) \times \Psi)^{1.130},$$

where Ψ is the color adjustment derived from Equation (4) and the values in Table 2.

Compared to pure starburst systems from the GOALS sample, this color-adjusted $\Sigma_{[\text{C II}]} - \Sigma_{\text{SFR}}$ correlation is valid over almost five orders of magnitude. We caution, however, that blind application of this calibration to systems that may host an AGN, or where enough information to determine or bracket the color adjustment Ψ is not available, risks a significant underestimate of the SFR.

For cases where no information on the size of the emitting object is available, we derive an SFR calibration (Equation (3)) based on the [C II] luminosity, $L_{[\text{C II}]}$. The dispersion in this correlation is similar to that of the $\Sigma_{[\text{C II}]} - \Sigma_{\text{SFR}}$ correlation. However, when compared to samples of galaxies with $L_{\text{TIR}} > 10^{11} L_{\odot}$, our $L_{[\text{C II}]}$ based calibration—even after applying the IR color adjustment—can underestimate the SFRs by more than a factor of ~ 3 . We suspect that the reason why the surface brightness calibration has better systematics is because it is more closely related to the local FUV field, most likely the main parameter controlling the photoelectric heating efficiency.

We highlight the following points.

1. We find a tight correlation between the surface brightness of [C II] and 24 μm dust emission in normal galaxies. Regions located in the central ~ 1 kpc of galaxies that show AGN activity tend to show an excess of 24 μm emission compared to [C II]. After excluding these points, the best linear fit yields a slope of 1.20 ± 0.01 (Calzetti et al. 2007, which is close to the slope measured by) [for the correlation between 24 μm and SFR]. The scatter of the correlation is ± 0.23 dex.

2. For each individual region in our galaxy sample, we estimate the contribution from old stars to the 24 μm dust emission using the procedure described in Leroy et al. (2012). We refer to this emission as cirrus. We assume that the radiation field produced by these older populations is $U_{\text{cirrus}} = 0.5 \times U_{\text{min}}$, where U_{min} corresponds to the least interstellar radiation field heating the diffuse ISM in the Draine & Li (2007) model. We find that the median 24 μm cirrus contribution across the sample is 18%. In order to obtain a more accurate measure of the SFR based on the 24 μm emission, we subtract from it our estimate of the cirrus contribution.
3. We estimate the SFR and Σ_{SFR} values for each region using a combination of obscured (24 μm and TIR) and unobscured SFR tracers (H α and FUV). We then derive calibrations for the Σ_{SFR} and SFR based on $L_{[\text{C II}]}$ and $\Sigma_{[\text{C II}]}$, respectively. The calibration coefficients can be found in Table 3. We find that, for $\nu f_{\nu}(70)/\nu f_{\nu}(160) \gtrsim 1.2$ or $\nu f_{\nu}(70)/\nu f_{\nu}(100) \gtrsim 0.8$, the fit residuals systematically increase with increasing IR color (dust temperature), radiation field strength, fraction of the luminosity coming from regions with $U > 100$, and decreasing q_{PAH} . At a slightly higher IR color threshold, $\nu f_{\nu}(70)/\nu f_{\nu}(100) \gtrsim 0.95$, Croxall et al. (2012) find a drop in the [C II] to FIR ratio for regions in NGC 4559 and NGC 1097. We parameterize the deviations we find for our warm regions as a function of IR color by a linear fit and derive a set of adjustments that reduces the residuals significantly. The list of IR color adjustments is given in Table 2.
4. For regions with oxygen abundances $12 + \log(\text{O}/\text{H}) \lesssim 8.1$, we find that our [C II]-based SFR calibration is not reliable. Regions from the low-metallicity galaxies Holmberg II, IC 2574 and NGC 5408 show [C II]-based SFRs that are a factor of ~ 4 smaller than their SFR measured as a combination of 24 μm and FUV emission for the first two systems, and 24 μm for NGC 5408. These regions not only have the highest dust temperatures in the sample, but they also show significantly higher FUV to TIR ratios than their metal-rich counterparts. This suggests that a larger fraction of FUV photons escapes without interacting with the dust. If the [C II] emission is mainly produced by grain photoelectric emission—which requires FUV absorption by dust—then the reduced trapping of FUV photons would explain the low [C II]-based SFRs observed in low-metallicity regions. In addition to this, we find that in NGC 5408 the [O I] 63 μm to [C II] line ratio can be as high as ~ 1 , thus the cooling can be equally split between these two FIR transitions. For this particular galaxy, an SFR estimated from [C II] alone will underpredict the total SFR by a factor of two. The line ratios and upper limits in Holmberg II and IC 2574 do not rule out a similar scenario for these objects.
5. We find that an IR-color-adjusted $\Sigma_{[\text{C II}]}$ can provide a good estimation of Σ_{SFR} using Equation (2), valid for starburst galaxies over almost five orders of magnitude in surface brightness. Without applying the IR color adjustment, KINGFISH regions and starbursts systems with $L_{\text{FIR}} \leq 10^{11} L_{\odot}$ agree within a factor of ~ 2 with Equation (2). Starbursts with $L_{\text{FIR}} \geq 10^{11} L_{\odot}$ tend to follow the same trend, but with Σ_{SFR} values that are, on average, a factor of ~ 3 higher for a given $\Sigma_{[\text{C II}]}$.
6. In the luminosity regime, the SFR calibration defined by Equation (3) works well for samples of normal,

star-forming galaxies (Boselli et al. 2002; De Looze et al. 2011), but underestimates the SFR derived from the TIR value by a factor greater than ~ 3 for more than half of the GOALS galaxies and non-AGN LIRGs (Sargsyan et al. 2012; B. Weiner et al. in preparation). The IR color adjustment helps to reduce the discrepancy—especially for the GOALS sample—but even after applying the adjustment there are LIRGs that show deviations as high as a factor of ~ 10 . This demonstrates the limitations of using the [C II] luminosity as an SFR measure in warm or compact IR luminous and ultra luminous galaxies, for which low [C II] to TIR ratios—or the so called [C II]-deficit—have been extensively reported in the literature. One additional factor behind these deviations is the different tracers we are using to measure the SFR of LIRGs (TIR) and the KINGFISH regions ($24\ \mu\text{m}$ combined with H α or FUV). Interestingly, we find that if we measure the SFR of LIRGs using monochromatic IR-based SFR tracers (e.g., $24\ \mu\text{m}$), the agreement with the SFR inferred from [C II] through our calibration is considerably better.

7. We use the *Starburst99* code to connect the FUV luminosity of modeled stellar populations to the [C II] emission via the heating efficiency, ϵ_h . We find that the [C II] emission from most of the galaxies can be attributed to regions that have been forming stars continuously for more than 20 Myr in combination with a heating efficiency in the range $\epsilon_h \sim 1\% - 3\%$. It appears likely that the variation in the latter drives much of the scatter in the [C II]–SFR correlation.

We thank the referee for constructive and valuable comments on the paper. R.H.C. acknowledges support from a Fulbright-CONICYT grant. A.D.B. acknowledges partial support from a CAREER grant NSF-AST0955836, from NSF-AST1139998, from NASA-JPL 1373858, and from a Research Corporation for Science Advancement Cottrell Scholar award. We thank B. Weiner for providing [C II] and FIR fluxes for his sample of LIRGs in advance of publication. We also thank T. Diaz-Santos for providing the areas used to measure the surface brightness of the galaxies in the GOALS sample in advance of publication. PACS has been developed by a consortium of institutes led by MPE (Germany) and including UVIE (Austria); KU Leuven, CSL, IMEC (Belgium); CEA, LAM (France); MPIA (Germany); INAF-IFSI/OAA/OAP/OAT, LENS, SISSA (Italy); IAC (Spain). This development has been supported by the funding agencies BMVIT (Austria), ESA-PRODEX (Belgium), CEA/CNES (France), DLR (Germany), ASI/INAF (Italy), and CICYT/MCYT (Spain). HIPE is a joint development by the Herschel Science Ground Segment Consortium, consisting of ESA, the NASA Herschel Science Center, and the HIFI, PACS, and SPIRE consortia. This work is based (in part) on observations made with *Herschel*, a European Space Agency Cornerstone Mission with significant participation by NASA. The National Radio Astronomy Observatory is a facility of the National Science Foundation operated under cooperative agreement by Associated Universities, Inc. This research has made use of the NASA/IPAC Extragalactic Database (NED), which is operated by the Jet Propulsion Laboratory, California Institute of Technology, under contract with the National Aeronautics and Space Administration.

We wish to dedicate this study to the memory of our colleague Dr. Charles “Chad” Engelbracht for his numerous contributions to space-based far-infrared astronomy that made this work

possible, as well as that of many other researchers employing *Spitzer* and *Herschel* observations.

APPENDIX A

KINGFISH GALAXIES NOT INCLUDED IN THE ANALYSIS

Among the 54 galaxies in the KINGFISH sample with PACS spectroscopic data available, we decided not to include eight of them: NGC 1266, NGC 1316, NGC 1097, NGC 1377, NGC 1404, NGC 4594, NGC 4631, and NGC 4559. We excluded the two elliptical galaxies NGC 1266 and NGC 1316 (also known as Fornax A) because they both have AGNs (Ekers et al. 1983; Moustakas et al. 2010; Nyland et al. 2013) that may contaminate the infrared emission used to measure SFRs. Unfortunately, masking the AGN emission at the center of these galaxies is not an option because it removes a significant fraction of the [C II] map. NGC 1377 is a peculiar system that shows a $24\ \mu\text{m} - [\text{C II}]$ ratio nearly two orders of magnitude higher than the rest of the points at a given [C II] surface brightness. The strong infrared excess in this system is produced either by a nascent starburst (Roussel et al. 2006) or a buried AGN (Imanishi et al. 2009). Given that the central source that dominates the emission of NGC 1377 is debated, we remove this system from the analysis. We also do not include NGC 1404 and NGC 4594 because the quality of the spectroscopic data is poor. We remove NGC 4631 from the sample because of its high inclination of 86° (Muñoz-Mateos et al. 2009a). Finally, we do not include NGC 1097 and NGC 4559 because these two galaxies were observed in the Science Demonstration Phase using a different observing mode (i.e., Chop-Nod and Wavelength Switching) than the one used to observe the rest of the sample (Unchopped Grating Scan). Note, however, that these two systems agree well with the correlations presented in this work.

APPENDIX B

SUPPLEMENTARY DATA

SINGS and KINGFISH IR. For all galaxies in our sample we have images that cover the entire IR continuum from $3.6\ \mu\text{m}$ to $500\ \mu\text{m}$. Near and mid-infrared (8 and $24\ \mu\text{m}$) images were drawn from the *Spitzer* Infrared Nearby Galaxy Survey (Kennicutt et al. 2003, ; SINGS). Far-infrared maps observed with *Herschel* PACS (70 , 100 , and $160\ \mu\text{m}$) and SPIRE (250 , 350 , and $500\ \mu\text{m}$) instruments are drawn from the photometric KINGFISH sample (Dale et al. 2012). We also add [O I] $63\ \mu\text{m}$ data reduced and calibrated in the same way as the [C II] data.

H α . We have H α images for 27 galaxies. The assembly of these images and the methods to correct for Galactic extinction, mask foreground stars and remove the [N II] contribution are described in detail in Leroy et al. (2012). The source of these images are (in order of importance): SINGS (Kennicutt et al. 2003); Local Volume Legacy (LVL) survey (Dale et al. 2009); GOLDMine (Gavazzi et al. 2003); Palomar Las Campanas Atlas (Boselli & Gavazzi 2002; Knapen et al. 2004; and Hoopes et al. 2001).

FUV. We have *GALEX* FUV images for 33 of the galaxies in our sample. The assembly of these images and the additional processing that includes background subtraction and masking of foreground stars via their UV color, by-eye inspection, and the color-based masks of Muñoz-Mateos et al. (2009b) is described in Leroy et al. (2012). The source of these images are (in order of

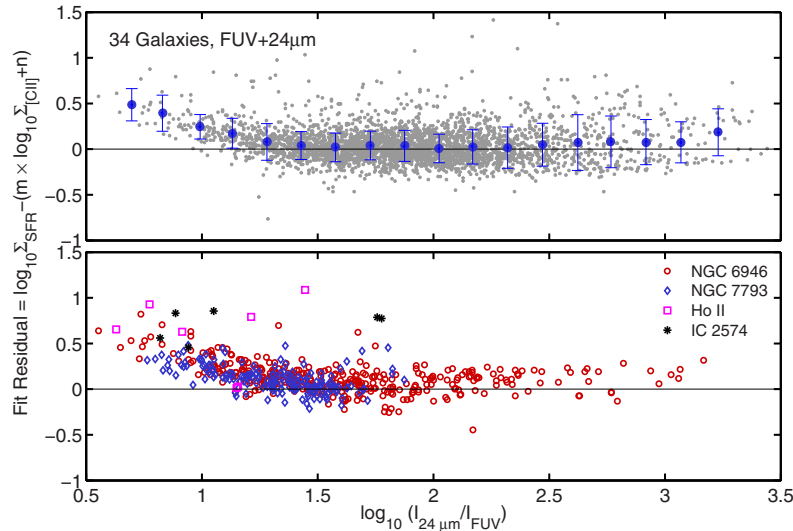


Figure 12. Fit residual of the $\Sigma_{[\text{C II}]} - \Sigma_{\text{SFR}}$ correlation as a function of the fraction of FUV absorbed and reprocessed by dust vs. the escaping FUV emission ($I_{24\mu\text{m}}/I_{\text{FUV}}$). Each point represent a $12''$ size region. Blue dots and the corresponding vertical bars correspond to the median and the 1σ standard deviation of the binned distribution of points. Top panel: for 33 galaxies for which we have FUV maps available, we measure Σ_{SFR} as a linear combination of $24\mu\text{m}$ and FUV emission (Leroy et al. 2008) and the dust attenuation as the ratio of the $24\mu\text{m}$ intensity, $I_{24\mu\text{m}}$ (MJy sr^{-1}), and the FUV intensity, I_{FUV} (MJy sr^{-1}). Bottom panel: four individual galaxy cases: two galaxies with global average low metallicity (Holmberg II and IC 2574) and two galaxies that are the main source of the low extinction regions that deviate from the fit (NGC 6946 and NGC 7793).

importance) the Nearby Galaxy Survey (Gil de Paz et al. 2007), Medium Imaging Survey, and All-sky Imaging Survey (Martin et al. 2005).

Draine & Li Dust Model Maps. We use maps of dust properties, like the ones presented in Aniano et al. (2012), based on the Draine & Li dust model (DL07). The DL07 model treats the dust as a combination of carbonaceous and amorphous silicate grains, with the smallest carbonaceous grains having the physical properties of PAH particles. The PAH mass fraction, q_{PAH} , is defined as the percentage of the total grain mass contributed by PAHs containing fewer than 10^3 C atoms (see Draine et al. 2007, Equation (4)). The grain size distribution and normalization is chosen to match the abundance and average extinction in the Milky Way. The DL07 model considers that dust is exposed to a range of radiation fields: a “diffuse ISM” component—that contains most of the dust—which is heated by a single (δ function) radiation field, $U = U_{\text{min}}$; and a “PDR component” that is heated by a power-law distribution of intensities U over a wide range, $U_{\text{min}} < U < U_{\text{max}}$, where ($U_{\text{max}} \gg U_{\text{min}}$). For the “PDR component,” the DL07 model estimate the fraction of the dust luminosity radiated from regions where $U > 100$ (see Draine et al. 2007, Equation (18)). Finally, the DL07 model also yields a dust mass (M_{dust}) and a dust mass surface density (Σ_{dust}) for each line of sight. In this paper we use the version of the dust maps generated by fitting the IR SED composed of the MIPS $24\mu\text{m}$ and PACS 70, 100, and $160\mu\text{m}$ fluxes. We use this version of the dust maps, as opposed to the version that include SPIRE fluxes, to have dust maps with similar spatial resolution to the [C II] $158\mu\text{m}$ maps.

APPENDIX C

CIRRUS EMISSION

Following the procedure described in Leroy et al. (2012), the $24\mu\text{m}$ cirrus intensity ($I_{24\mu\text{m}}^{\text{cirrus}}$) can be computed as the product of the dust surface density (Σ_{dust}), and the emission per unit dust mass of dust heated by non-star-forming sources ($\epsilon_{24}^{\text{cirrus}}$):

$$I_{24\mu\text{m}}^{\text{cirrus}} = \epsilon_{24}^{\text{cirrus}}(U_{\text{cirrus}}, q_{\text{PAH}}) \times \Sigma_{\text{dust}}. \quad (\text{C1})$$

In the DL07 model, ϵ_{24} depends linearly on the incident radiation field, U ($U = 1$ is the local interstellar radiation field in the Milky Way, normalized to the MMP field (Mathis et al. 1983)) and weakly on the PAH abundance index, q_{PAH} (Figure 4, Leroy et al. 2012). For instance, for a radiation field $U = 1$, the emission per unit dust mass ϵ_{24} increases only by a factor of ~ 1.75 in the $q_{\text{PAH}} = 0.47\% - 4.58\%$ range (DL07, Table 4). Therefore, the challenge here is to find the incident radiation field produced by non-star-forming sources, i.e., U_{cirrus} . Leroy et al. (2012) test different values of U_{cirrus} with the goal of producing $24\mu\text{m}$ cirrus emission such that its subtraction removes the $24\mu\text{m}$ faint emission, but not oversubtract emission associated with star formation. For a sample of 30 disk galaxies (20 of them part of the KINGFISH sample), they find that this optimal cirrus radiation field is $U_{\text{cirrus}} \approx 0.5 U_{\text{min}}$, where U_{min} corresponds—in the DL07 model—to the least interstellar radiation field heating the diffuse ISM. There is a factor of ~ 2 scatter associated with this value (Leroy et al. 2012; Appendix A).

We explore the effects of the cirrus subtraction estimating U_{cirrus} as a scaled version of U_{min} , i.e., $U_{\text{cirrus}} = \xi \times U_{\text{min}}$ for $\xi = 0.5, 0.75$ and 1 . We also explore adopting a constant U_{cirrus} across the galaxy. Given that we measure a median value of U_{min} in our sample of 1.15 , we adopt a constant $U_{\text{cirrus}} = \xi \times 1.15 = 0.6, 0.8$ and 1.1 . Choosing a high cirrus radiation field, such as $U_{\text{cirrus}} = U_{\text{min}}$ or $U_{\text{cirrus}} = 1.1$, will likely overestimate the cirrus emission. As Leroy et al. (2012) point out, the OB associations present within 1 kpc of the Sun would substantially contribute to the local interstellar radiation field, so non-star-forming sources—like old stars—cannot by themselves account on their own to the local measured value of $U = 1$.

Table 1 summarizes the effect of the cirrus correction on the $\Sigma_{24\mu\text{m}} - \Sigma_{[\text{C II}]}$ correlation and the fraction of the $24\mu\text{m}$ emission associated with cirrus (f_{cir}). When cirrus is estimated using $U_{\text{cirrus}} = 0.5 U_{\text{min}}$, the shape and scatter of the corrected correlation remains essentially the same, but the normalization scales down about 18% (as expected since $f_{\text{cir}} \sim 18\%$ for this case). For the cirrus removal based on $U_{\text{cirrus}} = 0.6$, the cirrus subtraction is higher at lower luminosities of $24\mu\text{m}$,

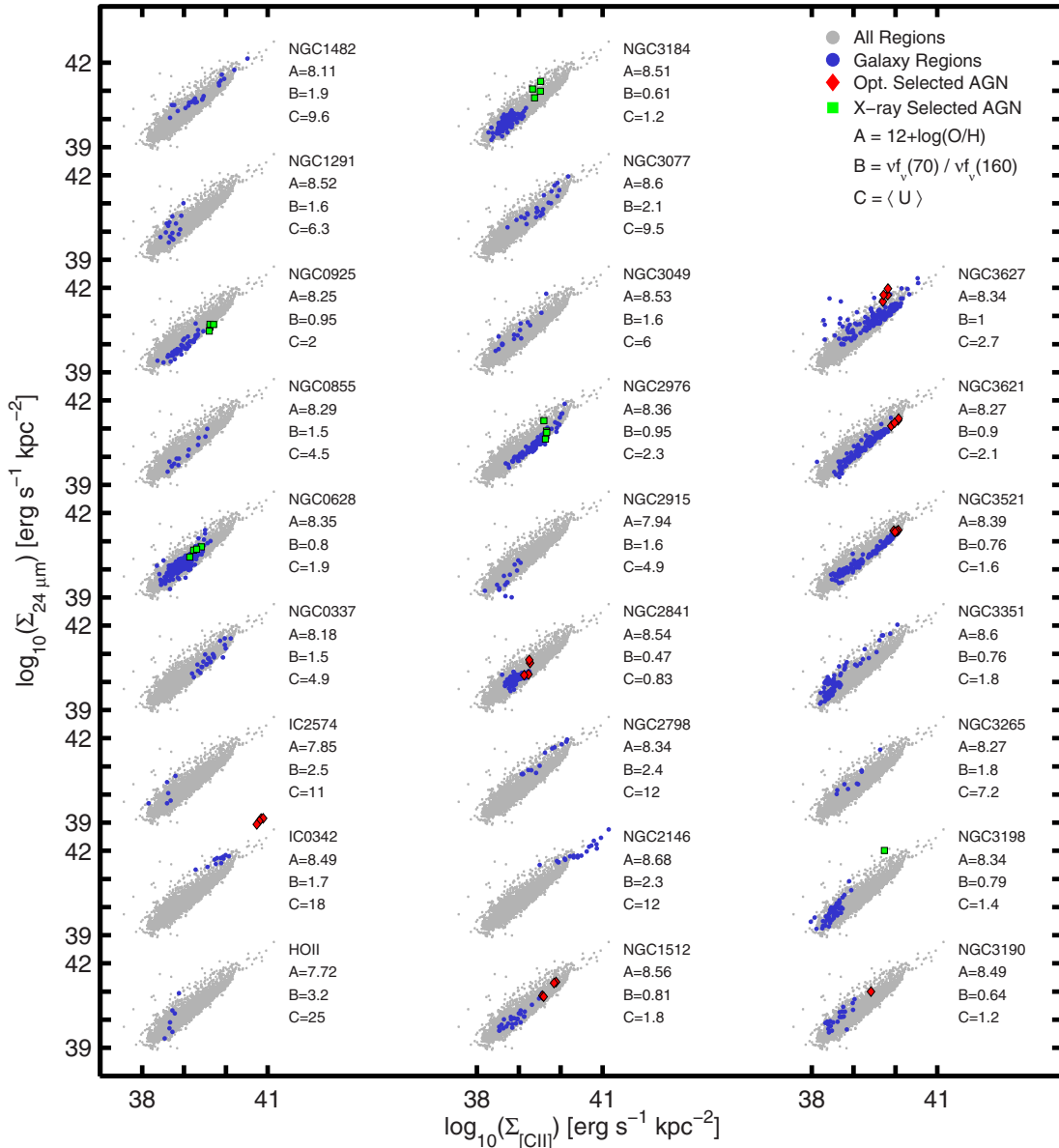


Figure 13. $[\text{C II}]$ luminosity surface density vs. $24\ \mu\text{m}$ surface density for each of the KINGFISH galaxies in our sample. The gray dots correspond to all the regions from the 46 KINGFISH galaxies in our sample. The blue dots correspond to the regions of the galaxy whose name is on the top right of the correlation. We also list the metallicity (A), mean IR color (B), and mean starlight intensity of the galaxy. If the galaxy hosts an AGN, the regions from the central ~ 0.5 kpc radius are shown as red diamonds for optically selected AGNs (Moustakas et al. 2010) and green squares for X-ray-selected AGNs (Tajer et al. 2005; Grier et al. 2011).

thus we observe an increase in the slope from 1.20 to 1.30; the scatter of the correlation remains the same. For these two sets of assumptions on U_{cirrus} , the median f_{cir} is similar to the $f_{\text{cir}} \sim 19\%$ found by Leroy et al. (2012; the overlap between our samples is 23 galaxies) and larger than the $f_{\text{cir}} \sim 7\%$ found by Law et al. (2011) in their analysis of integrated SEDs for LVL and SINGS galaxies. For the $U_{\text{cirrus}} = 1.1$ case, the changes in the correlation after the cirrus removal are more dramatic: the slope changes from 1.20 to 1.60; as a result, the subtracted $24\ \mu\text{m}$ emission in the low $[\text{C II}]$ luminosity regions ($\Sigma_{[\text{C II}]} < 10^{39}$ ($\text{erg s}^{-1} \text{kpc}^{-2}$)) can be a factor of ~ 2 smaller compared to the uncorrected correlation.

APPENDIX D

DUST ATTENUATION

Another physical variable of interest in the analysis of the local variations is the dust attenuation. For 33 galaxies for

which we have FUV images available, we measure the fraction of FUV and optical emission absorbed and reprocessed by dust versus the escaping FUV emission as the ratio of the $24\ \mu\text{m}$ to the FUV intensity, $I_{24\ \mu\text{m}}/I_{\text{FUV}}$. Figure 12 shows the residuals of the correlation between the $[\text{C II}]$ -based Σ_{SFR} and $\Sigma_{\text{SFR}}(\text{FUV}+24\ \mu\text{m})$. The top panel shows the fit residuals for all the $12''$ regions from the 33 galaxies for which we have FUV maps available. Around the $I_{24\ \mu\text{m}}/I_{\text{FUV}}$ ratio of ~ 10 , we observe a systematic increase of the fit residuals as a function of decreasing extinction. The bottom panel of Figure 12 shows that the regions that deviate are mainly coming from two galaxies: NGC 6946 and NGC 7793. Visual inspection of the $[\text{C II}]$ and dust attenuation maps reveals that the regions with low $I_{24\ \mu\text{m}}/I_{\text{FUV}}$ ratios are located preferentially in regions of low surface brightness in the “extranuclear” pointings. The rest of the regions that show high fit residuals at low $I_{24\ \mu\text{m}}$ to I_{FUV} ratios are from the low-metallicity systems ($12+\log_{10}(\text{O}/\text{H}) < 8.1$) Holmberg II and IC 2574.

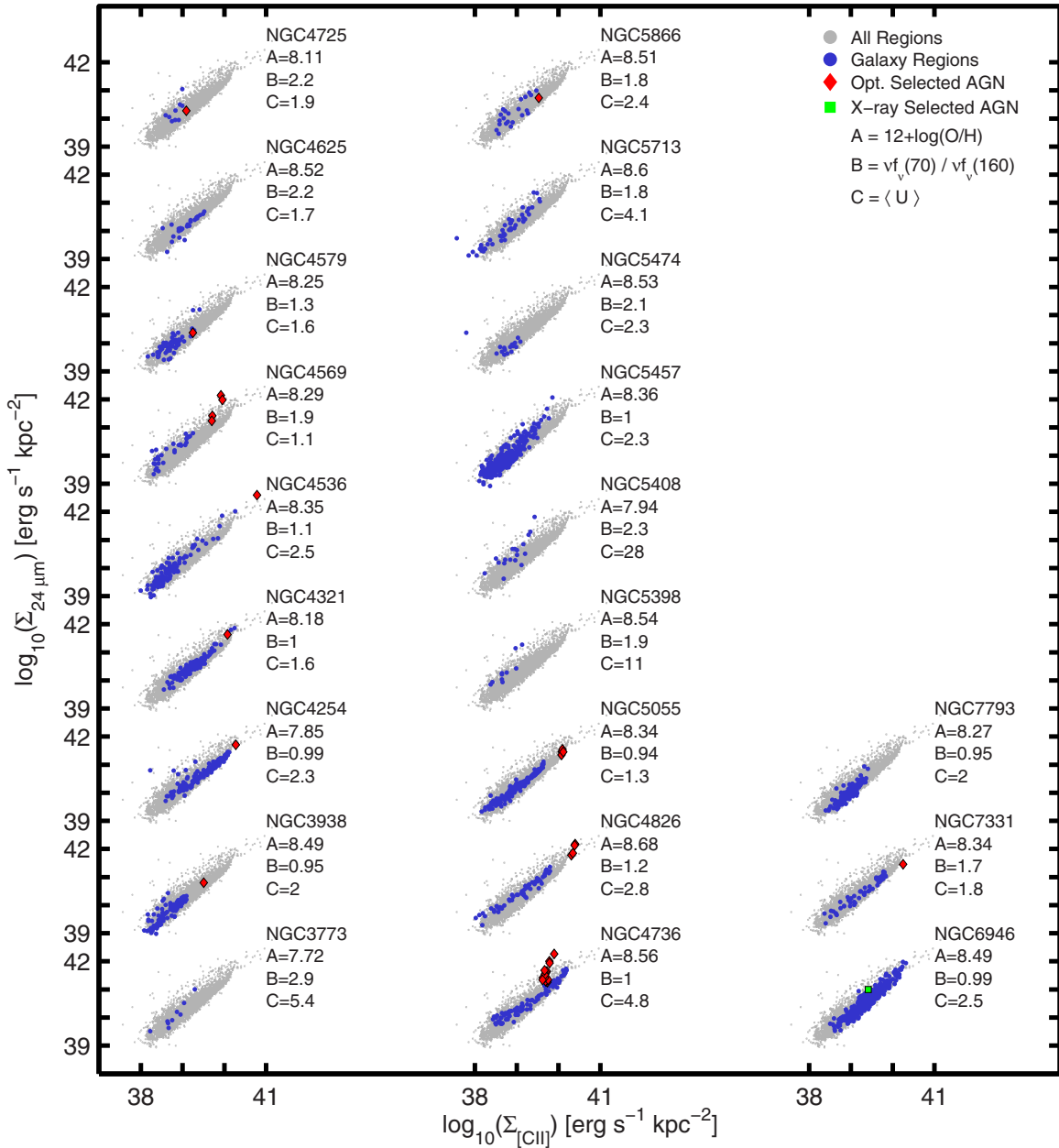


Figure 14. Same as Figure 13.

APPENDIX E

ADDITIONAL SAMPLES OF GALAXIES
INCLUDED IN OUR ANALYSIS

Díaz-Santos et al. (2013). From the 241 systems comprising the GOALS sample, we only select a subset of 116 systems that are classified as pure starburst following the criteria described in *Díaz-Santos et al. (2013)*, i.e., those which have $6.2\ \mu\text{m}$ PAH equivalent widths that are greater than 0.5. The sample covers a distance range of $\sim 16\text{--}350$ Mpc. We compiled PACS [C II] flux densities, [C II] to FIR ratios and PACS continuum flux densities at 63 and $158\ \mu\text{m}$ under the [O I] and [C II] lines, respectively, from *Díaz-Santos et al. (2013)*. The areas of the infrared emitting nuclear regions of the GOALS sample were provided by T. Díaz-Santos (2014, private communication).

The FIR luminosities in *Díaz-Santos et al. (2013)* were measured based on the 60 and $100\ \mu\text{m}$ IRAS bands using Helou

et al. (1988) calibration. In order to use the SFR calibration by Murphy et al. (2011) (or Kennicutt (1998), which yields an SFR value ~ 1.3 times higher), we need to convert these FIR ($60\text{--}100\ \mu\text{m}$) luminosities into TIR ($8\text{--}1000\ \mu\text{m}$) luminosities. The ideal would be to measure the TIR luminosity of the GOALS galaxies by integrating their SED from 8 to $1000\ \mu\text{m}$. This can be done for 64 U/LIRGs from the GOALS sample, for which U et al. (2012) compiled aperture photometry from radio through X-ray wavelengths. Based on these SEDs, U et al. (2012) use different dust models and a modified blackbody fit to measure the TIR luminosity from 8 to $1000\ \mu\text{m}$. They find that these integrated TIR ($8\text{--}1000\ \mu\text{m}$) luminosities are about 0.02 dex lower than the FIR ($12\text{--}100\ \mu\text{m}$) luminosities measured using the calibration by Sanders & Mirabel (1996). Compared to the FIR ($60\text{--}100\ \mu\text{m}$) luminosities based on the Helou et al. (1988) calibration, the TIR ($8\text{--}1000\ \mu\text{m}$) luminosities are higher by a factor of 1.74. We adopt this factor to convert the FIR luminosities listed in *Díaz-Santos et al. (2013)* into

TIR (8–1000 μm) luminosities, and then we measure the SFR based on TIR (8–1000 μm) using the calibration by Murphy et al. (2011).

Boselli et al. (2002). This work encompasses 23 galaxies detected in [C II] line emission by *ISO*. The sample include 18 spiral systems from the Virgo Cluster ($D = 17$ Mpc). The [C II], H α and FIR luminosities were taken from the paper. Additional IRAS 60 and 100 μm fluxes were added from Leech et al. (1999) and Smith & Madden (1997). We measure the SFR from the H α luminosities using the Calzetti et al. (2007) calibration. In order to derive individual IR color adjustments, we interpolate the value of the 70 μm flux based in the 60 and 100 μm fluxes, and then we measure the 70/100 μm ratio for each galaxy.

De Looze et al. (2011). This work encompasses 17 star-forming and starburst galaxies observed by *ISO* and located within 60 Mpc, with the exception of one system that is 139 Mpc away. The [C II], 24 μm , FUV, and FIR luminosities were taken from the paper. We measure the SFR as a combination of 24 μm and FUV emission using the Leroy et al. (2008) calibration. For the IR color adjustment, we compile 60 and 100 μm fluxes from Brauher et al. (2008). Based on interpolated values of the 70 μm flux, we measure the 70/100 μm ratio for each galaxy in the sample.

Sargsyan et al. (2012). This work includes 23 starbursting LIRGs observed by *Herschel* and located in the distance range from ~ 66 to 505 Mpc. We compiled [C II] and FIR (12–100 μm) luminosities from their paper. As we mentioned in Section 4.2, the FIR (12–100 μm) luminosities measured using Sanders & Mirabel (1996) calibration are similar to the integrated TIR (8–1000 μm) luminosities in U/LIRGs (U et al. 2012). Therefore, we use the FIR (12–100 μm) luminosities to measure the SFR based on Murphy et al. (2011) calibration.

B. Weiner et al. (2013, in preparation). This work includes 16 disk non-mergers, non-AGNs, LIRGs located at $z \sim 0.1$. The [C II] 158 μm , 60 and 100 μm IRAS fluxes were provided by B. Weiner (private communication). We measure the FIR luminosities using the 60 and 100 μm fluxes. We then measure the TIR luminosities, SFRs, and 70/100 μm IR colors using the same procedure applied to the Díaz-Santos et al. (2013) sample.

APPENDIX F

$\Sigma_{[\text{C II}]} - \Sigma_{24\mu\text{m}}$ CORRELATION FOR THE KINGFISH GALAXIES

In Figures 13 and 14, we present individual correlations between the [C II] and 24 μm luminosity surface densities for each of the galaxies in our sample. For the systems that host an AGN, the diamonds mark the regions selected from the central ~ 0.5 kpc radius aperture. Next to each correlation, we also list the global metallicity, mean IR color, and mean starlight intensity of the galaxy.

REFERENCES

- Aniano, G., Draine, B. T., Gordon, K. D., & Sandstrom, K. 2011, *PASP*, 123, 1218
- Aniano, G., Draine, B. T., Calzetti, D., et al. 2012, *ApJ*, 756, 138
- Armus, L., Mazzarella, J. M., Evans, A. S., et al. 2009, *PASP*, 121, 559
- Beirão, P., Armus, L., Helou, G., et al. 2012, *ApJ*, 751, 144
- Bennett, C. L., Fixsen, D. J., Hinshaw, G., et al. 1994, *ApJ*, 434, 587
- Boselli, A., & Gavazzi, G. 2002, *A&A*, 386, 124
- Boselli, A., Gavazzi, G., Lequeux, J., & Pierini, D. 2002, *A&A*, 385, 454
- Brauher, J. R., Dale, D. A., & Helou, G. 2008, *ApJS*, 178, 280
- Calzetti, D., Kennicutt, R. C., Engelbracht, C. W., et al. 2007, *ApJ*, 666, 870
- Cormier, D., Leboutteiller, V., Madden, S. C., et al. 2012, *A&A*, 548, A20
- Cormier, D., Madden, S. C., Hony, S., et al. 2010, *A&A*, 518, L57
- Crawford, M. K., Genzel, R., Townes, C. H., & Watson, D. M. 1985, *ApJ*, 291, 755
- Croxall, K. V., Smith, J. D., Brandl, B. R., et al. 2013, *ApJ*, 777, 96
- Croxall, K. V., Smith, J. D., Wolfire, M. G., et al. 2012, *ApJ*, 747, 81
- Dale, D. A., Aniano, G., Engelbracht, C. W., et al. 2012, *ApJ*, 745, 95
- Dale, D. A., Cohen, S. A., Johnson, L. C., et al. 2009, *ApJ*, 703, 517
- Dale, D. A., Gil de Paz, A., Gordon, K. D., et al. 2007, *ApJ*, 655, 863
- Dale, D. A., Smith, J. D. T., Armus, L., et al. 2006, *ApJ*, 646, 161
- De Looze, I., Baes, M., Bendo, G. J., Cortese, L., & Fritz, J. 2011, *MNRAS*, 416, 2712
- De Looze, I., Cormier, D., Leboutteiller, V., et al. 2014, *A&A*, 568, A62
- Deo, R. P., Richards, G. T., Crenshaw, D. M., & Kraemer, S. B. 2009, *ApJ*, 705, 14
- Díaz-Santos, T., Armus, L., Charmandaris, V., et al. 2013, *ApJ*, 774, 68
- Draine, B. T., Aniano, G., Krause, O., et al. 2014, *ApJ*, 780, 172
- Draine, B. T., Dale, D. A., Bendo, G., et al. 2007, *ApJ*, 663, 866
- Draine, B. T., & Li, A. 2007, *ApJ*, 657, 810
- Ekers, R. D., Goss, W. M., Wellington, K. J., et al. 1983, *A&A*, 127, 361
- Gavazzi, G., Boselli, A., Donati, A., Franzetti, P., & Scodreggio, M. 2003, *A&A*, 400, 451
- Gil de Paz, A., Boissier, S., Madore, B. F., et al. 2007, *ApJS*, 173, 185
- Goldsmith, P. F., Langer, W. D., Pineda, J. L., & Velusamy, T. 2012, *ApJS*, 203, 13
- Graciá-Carpio, J., Sturm, E., Hailey-Dunsheath, S., et al. 2011, *ApJL*, 728, L7
- Grier, C. J., Mathur, S., Ghosh, H., & Ferrarese, L. 2011, *ApJ*, 731, 60
- Groves, B., Krause, O., Sandstrom, K., et al. 2012, *MNRAS*, 426, 892
- Haffner, L. M., Dettmar, R.-J., Beckman, J. E., et al. 2009, *RvMP*, 81, 969
- Haffner, L. M., Reynolds, R. J., & Tuftes, S. L. 1999, *ApJ*, 523, 223
- Heiles, C. 1994, *ApJ*, 436, 720
- Heiles, C., & Troland, T. H. 2003, *ApJ*, 586, 1067
- Helou, G., Khan, I. R., Malek, L., & Boehmer, L. 1988, *ApJS*, 68, 151
- Helou, G., Malhotra, S., Hollenbach, D. J., Dale, D. A., & Contursi, A. 2001, *ApJL*, 548, L73
- Hollenbach, D. J., & Tielens, A. G. G. M. 1999, *RvMP*, 71, 173
- Hoopes, C. G., Walterbos, R. A. M., & Bothun, G. D. 2001, *ApJ*, 559, 878
- Hunter, D. A., Kaufman, M., Hollenbach, D. J., et al. 2001, *ApJ*, 553, 121
- Imanishi, M., Nakanishi, K., Tamura, Y., & Peng, C.-H. 2009, *AJ*, 137, 3581
- Isobe, T., Feigelson, E. D., Akritas, M. G., & Babu, G. J. 1990, *ApJ*, 364, 104
- Israel, F. P., & Maloney, P. R. 2011, *A&A*, 531, A19
- Joseph, R. D., Wright, G. S., & Prestwich, A. H. 1986, in *New Insights in Astrophysics. Eight Years of UV Astronomy with IUE*, ed. E. J. Rolfe (ESA SP-263; Noordwijk: ESA), 597
- Kennicutt, R. C., Bendo, G., Engelbracht, C., et al. 2003, *BAAS*, 35, 1351
- Kennicutt, R. C., Calzetti, D., Aniano, G., et al. 2011, *PASP*, 123, 1347
- Kennicutt, R. C., & Evans, N. J. 2012, *ARA&A*, 50, 531
- Kennicutt, R. C., Jr. 1983, *ApJ*, 272, 54
- Kennicutt, R. C., Jr. 1998, *ApJ*, 498, 541
- Kennicutt, R. C., Jr., Hao, C.-N., Calzetti, D., et al. 2009, *ApJ*, 703, 1672
- Knapen, J. H., Stedman, S., Bramich, D. M., Folkes, S. L., & Bradley, T. R. 2004, *A&A*, 426, 1135
- Kobulnicky, H. A., & Kewley, L. J. 2004, *ApJ*, 617, 240
- Law, K.-H., Gordon, K. D., & Misselt, K. A. 2011, *ApJ*, 738, 124
- Leech, K. J., Völk, H. J., Heinrichsen, I., et al. 1999, *MNRAS*, 310, 317
- Leitherer, C., Schaerer, D., Goldader, J. D., et al. 1999, *ApJS*, 123, 3
- Leroy, A. K., Bigiel, F., de Blok, W. J. G., et al. 2012, *AJ*, 144, 3
- Leroy, A. K., Walter, F., Brinks, E., et al. 2008, *AJ*, 136, 2782
- Luhman, M. L., Satyapal, S., Fischer, J., et al. 1998, *ApJL*, 504, L11
- Luhman, M. L., Satyapal, S., Fischer, J., et al. 2003, *ApJ*, 594, 758
- Madden, S. C., Poglitsch, A., Geis, N., Stacey, G. J., & Townes, C. H. 1997, *ApJ*, 483, 200
- Madden, S. C., Rémy-Ruyer, A., Galametz, M., et al. 2013, *PASP*, 125, 600
- Malhotra, S., Helou, G., Stacey, G., et al. 1997, *ApJL*, 491, L27
- Malhotra, S., Kaufman, M. J., Hollenbach, D., et al. 2001, *ApJ*, 561, 766
- Maloney, P. R., Hollenbach, D. J., & Tielens, A. G. G. M. 1996, *ApJ*, 466, 561
- Martin, D. C., Fanson, J., Schiminovich, D., et al. 2005, *ApJL*, 619, L1
- Mathis, J. S., Mezger, P. G., & Panagia, N. 1983, *A&A*, 128, 212
- McKee, C. F., & Ostriker, J. P. 1977, *ApJ*, 218, 148
- McKee, C. F., & Williams, J. P. 1997, *ApJ*, 476, 144
- Mookerjee, B., Kramer, C., Buchbender, C., et al. 2011, *A&A*, 532, A152
- Moustakas, J., Kennicutt, R. C., Jr., Tremonti, C. A., et al. 2010, *ApJS*, 190, 233
- Muñoz-Mateos, J. C., Gil de Paz, A., Boissier, S., et al. 2009a, *ApJ*, 701, 1965
- Muñoz-Mateos, J. C., Gil de Paz, A., Zamorano, J., et al. 2009b, *ApJ*, 703, 1569
- Murphy, E. J., Condon, J. J., Schinnerer, E., et al. 2011, *ApJ*, 737, 67
- Nyland, K., Alatalo, K., Wrobel, J. M., et al. 2013, *ApJ*, 779, 173
- Pineda, J. L., Langer, W. D., & Goldsmith, P. F. 2014, *A&A*, 570, A121

- Pineda, J. L., Langer, W. D., Velusamy, T., & Goldsmith, P. F. 2013, *A&A*, **554**, A103
- Poglitsch, A., Krabbe, A., Madden, S. C., et al. 1995, *ApJ*, **454**, 293
- Povich, M. S., Stone, J. M., Churchwell, E., et al. 2007, *ApJ*, **660**, 346
- Rieke, G. H., Alonso-Herrero, A., Weiner, B. J., et al. 2009, *ApJ*, **692**, 556
- Roussel, H., Helou, G., Smith, J. D., et al. 2006, *ApJ*, **646**, 841
- Rubin, D., Hony, S., Madden, S. C., et al. 2009, *A&A*, **494**, 647
- Salim, S., Rich, R. M., Charlot, S., et al. 2007, *ApJS*, **173**, 267
- Sanders, D. B., & Mirabel, I. F. 1996, *ARA&A*, **34**, 749
- Sargsyan, L., Lebouteiller, V., Weedman, D., et al. 2012, *ApJ*, **755**, 171
- Shibai, H., Okuda, H., Nakagawa, T., et al. 1991, *ApJ*, **374**, 522
- Smith, B. J., & Madden, S. C. 1997, *AJ*, **114**, 138
- Stacey, G. J., Geis, N., Genzel, R., et al. 1991, *ApJ*, **373**, 423
- Stacey, G. J., Hailey-Dunsheath, S., Ferkinhoff, C., et al. 2010, *ApJ*, **724**, 957
- Stacey, G. J., Viscuso, P. J., Fuller, C. E., & Kurtz, N. T. 1985, *ApJ*, **289**, 803
- Stewart, S. G., & Walter, F. 2000, *AJ*, **120**, 1794
- Tajer, M., Trinchieri, G., Wolter, A., et al. 2005, *A&A*, **435**, 799
- U, V., Sanders, D. B., Mazzarella, J. M., et al. 2012, *ApJS*, **203**, 9
- Velusamy, T., Langer, W. D., Pineda, J. L., & Goldsmith, P. F. 2012, *A&A*, **541**, L10
- Walter, F., Kerp, J., Duric, N., Brinks, E., & Klein, U. 1998, *ApJL*, **502**, L143
- Weingartner, J. C., & Draine, B. T. 2001, *ApJS*, **134**, 263
- Wolfire, M. G., McKee, C. F., Hollenbach, D., & Tielens, A. G. G. M. 2003, *ApJ*, **587**, 278
- Wright, E. L., Mather, J. C., Bennett, C. L., et al. 1991, *ApJ*, **381**, 200